Charles University in Prague
Faculty of Mathematics and Physics

DIPLOMA THESIS

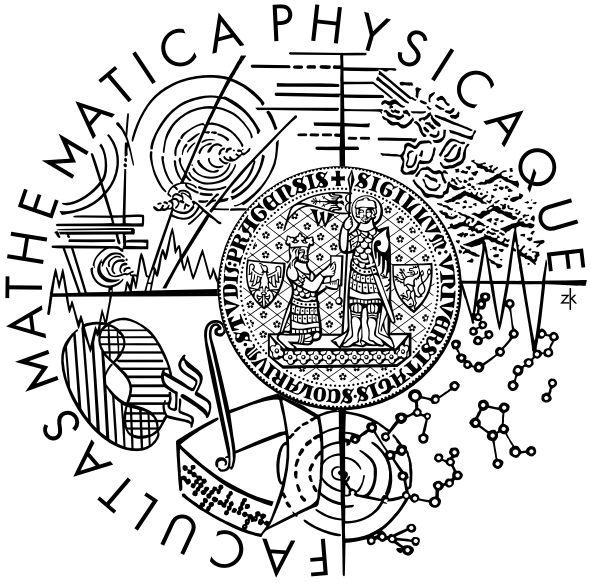

Boris Pokorný

Measurement of Properties of Calibration and Monitoring System for AHCAL

Institute of Particle and Nuclear Physics
Supervisor: RNDr. Jaroslav Zálešák, PhD.
Study programme: Physics, Nuclear and Subnuclear Physics

Acknowledgements

I would like to express my great gratitude to my supervisor RNDr. Jaroslav Zálešák for his patience he had with me when leading this thesis, for his professional feedback and help during my work.

I would like to thank also to Ing. Ivo Polák for helpful discussions on related technical issues and to Ing. Jaroslav Cvach for correction of the text and many worth suggestions. My word of thanks belongs also to Dr. Erika Garutti who introduced me into the problematics of calorimetry within the FLC group in DESY.

In a special way I would like to thank to my parents for their support over the last years.

I declare that I wrote my diploma thesis independently and exclusively with the use of the cited sources. I agree with lending this thesis.

Prague, 10th August 2007 Boris Pokorný

Contents

Title:	Measurement of Properties of Calibration and Monitoring System for AHCAL
Author:	Boris Pokorný
Department:	Institute of Particle and Nuclear Physics
Supervisor:	RNDr. Jaroslav Zálešák, PhD., Institute of Physics AS CR
supervisor's e-mai:	zalesak@fzu.cz

Abstract: This diploma thesis deals with tests of light emission diodes (LED) which are a basic element of a calibration and monitoring system for a hadronic calorimeter of a foreseen detector for the International Linear Collider (ILC). First part of the thesis consists of a brief overview of the ILC detector and focuses on the analogue version of the hadronic calorimeter (AHCAL). Main subsystems of the detector like trackers, calorimeters, muon system, etc. are described. The monitoring and calibration system designed for the HCAL is discussed in more detail. The main contribution of this thesis to the HCAL development consists in a selection test taken with a sample of UV-light LEDs. Not all of the LEDs contained in the sample are sufficient for usage in the calibration and monitoring system due to possible emitted light intensity variations. A dedicated experimental setup involving optical fibers and photo-detectors was constructed for the purpose of the selection.

Keywords: International Linear Collider, Particle Flow Approach, Analogue Hadronic Calorimeter, Control and Monitoring System, LED Selection Test

Název práce:	Měření vlastností kalibračního a kontrolního systému pro AHCAL
Autor:	Boris Pokorný
Katedra (Ústav):	Ústav částicové a jaderné fyziky
Vedoucí diplomové práce:	RNDr. Jaroslav Zálešák, PhD., Fyzikální ústav AV ČR
e-mail vedoucího:	zalesak@fzu.cz

Abstrakt: Tato diplomová práce pojednává o testech LED diod, které jsou základem kontrolního a kalibračního systému v novém hadronovém kalorimetru detektoru budoucího urychlovače ILC. První část práce podává stručný popis jednotlivých částí detektoru se zaměřením na analogovou verzi kalorimetru (AHCAL). Hlavní příspěvek této práce k vývoji AHCALu spočívá ve výběrovém testu, který byl prováděn se vzorkem ultrafialových LED diod. Vzhledem k možným odchylkám v intenzitě vyzařovaného světla nejsou všechny diody obsažené ve vzorku použitelné v kalibračním a kontrolním systému. Za účelem provedení výběru byla sestavena měřící aparatura obsahující optická vlákna a fotodetektory.

Klíčová slova: urychlovač ILC (z anglického 'International Linear Collider'), PFA (z anglického 'Particle Flow Approach'), analogový hadronový kalorimetr, kalibrační a kontrolní systém, výběrový test LED

Chapter 1

ILC Project

1.1 Introduction

This chapter deals with the physical motivation for building a new particle accelerator and give some technical aspects of the foreseen machine.

At the current stage of our understanding of the internal structure of matter we are left with a descriptive framework known as the standard model (SM). Ideas that form the basis of the SM consist in understanding interrelationships between the fundamental forces of nature. The formalism of the quantum field theory enable us to describe the electromagnetism, the weak force and the strong force be means of so called gauge theories where the interactions between the elementary particles are mediated via force-carrying particles - the gauge bosons. Thus the strong force that binds the nuclei is mediated by a set of eight gluons, the electromagnetic force by the photons (γ) and the weak force that is responsible for the radioactive decays by the $W^{\pm}$ and Z bosons. These particles have spin equal to one and are primordially massless. However, considering the short range of the weak interaction the $W^{\pm}$ and Z must be quite massive whereas their mass is generated through their interaction with a new Higgs field. Although from the theoretical view the required masses are well predicted the puzzle of the weak force carriers is left with a new, yet unseen, particle - the Higgs boson. The Higgs boson observation is a question of reaching sufficiently high collision energy since its mass is predicted to be larger than 114 GeV.

Not only the discovery and revealing the character of the Higgs boson brings challenge to increase the collision energy available at current accelerators. There are strong signals for possible new discoveries beyond the SM. Grand unification of the forces is suggested at about 10^{16} GeV where the strength of the electromagnetic, strong and weak force became similar. The exact unification cannot be reached by means of the simple SM. Moreover there exist so called hierarchy problem; at 10^{19} GeV (Plank scale) where the strength of gravity is comparable to the three remaining forces the extreme disparity with the electroweak scale occurs. In the SM the masses of the intermediate bosons are unstable to quantum fluctuations. Some new physics at 100 - 1000 GeV scale is necessary otherwise the masses of the $W^{\pm}$, Z and Higgs bosons would rise to the Plank Scale. From this point of view new phenomena are expected at the TeV scale. There is an option of existence of supersymmetry, e.g. new space and time coordinates and consequently the presence of supersymmetric particles which are nearly identical partners of currently known particles. In this theory each fermion carrying 1/2 of intrinsic spin should be accompanied by a superpartner with bosonic character (carrying a 0 or 1 spin) and on the other hand the known bosons are expected to have fermionic partners.

Yet uncompleted puzzle of the SM as well as exploring the new physics beyond its limits had led to a world-wide consensus in forming a baseline e^+e^- linear collider project with CMS energy up to 500 GeV further upgradeable to 1 TeV. The project is commonly known as the International Linear Collider (ILC). The data from the ILC will be necessary to provide the full picture of observation that are expected at the Large Hadron Collider (LHC), another next generation accelerator that is foreseen to start its operation at CERN during

the next year.

1.2 Physics at ILC

Next paragraphs are dedicated to observations expected at the ILC especially the possible discovery of the Higgs boson, non-standard model extensions of Higgs physics, revealing of supersymmetric particles, precision measurements and link to cosmology. The selected topics are discussed in more detail in Part III of [1].

1.2.1 Higgs Boson

The Higgs boson is a product of Higgs mechanism through which the fundamental particles (leptons, quarks and gauge bosons) acquire their masses. The mass generation is based on interaction with a scalar field of non-zero field strength v in its ground state (the non-zero v also stands behind the spontaneous symmetry breaking). In the SM one doublet of complex scalar fields is required in order to form the Higgs sector. The field strength of the ground state is obtained from the two fields self-interaction as $v = (\sqrt{2}G_F)^{-1/2} \approx 246$ GeV and the electroweak symmetry $SU(2) \times U(1)$ is broken to the electromagnetic symmetry $U(1)$. Within the Higgs mechanism the $W^{\pm}$ and Z bosons absorb three of the four initial degrees of freedom while the remaining one corresponds to a real scalar particle H^0-the Higgs boson. The scalar doublet is coupled to the fermions and gauge bosons via Yukawa interaction. Thus the corresponding coupling constants are uniquely determined by known SM parameters:

$$g_{ffH} = m_f/v, \; g_{VVH} = 2M_V^2/v \tag{1.1}$$

with m_f, M_V being fermion and gauge boson mass, respectively.

The mass of the Higgs boson M_H cannot be determined in the SM and it remains a free parameter of the theory. This parameter is closely related to the energy cut-off Λ: for small values of M_H (less then 200 GeV)the energy at which the couplings diverge is large and the SM is extendable to the grand unification scale, $\Lambda_{GUT} \sim 10^{16}$ GeV, or even the Planck scale, $\Lambda \sim 10^{19}$ GeV. On the other hand large values of M_H lead to significant decrease of Λ.

The requirement of vacuum stability provides a lower bound on M_H. The Higgs mass should be sufficiently high in order to balance contributions from top quark loop otherwise the corrections to the Higgs potential turns the self-interaction coupling constants into negative values and consequently the electroweak vacuum becomes unstable. According to [2] the SM Higgs mass lies in range $130 \leq M_H \leq 180$ GeV with the top quark mass about 175 GeV. An upper bound for M_H can be obtained from the unitarity requirement of scattering processes of the intermediate bosons. For instance, applying the unitarity requirement on the elastic scattering of longitudinal W bosons yields the upper bound for M_H to be less than 870 GeV [3]. Let us assume an extremely

heavy Higgs boson with $M_H \sim 1$ TeV. In such a case the electroweak intermediate bosons should interact strongly otherwise the unitarity is lost and this is incongruous with the perturbation theory.

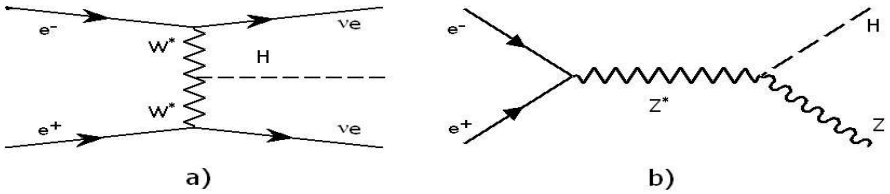

Figure 1.1: Main production mechanism of the SM Higgs boson at e^+e^- collision: a) WW fusion process, b) Higgs-strahlung process

There are basically two ways of the SM Higgs production in e^+e^- collision: first the WW fusion $e^+e^- \to W^*W^* \to \nu_e\overline{\nu}_e H$ that is dominant at higher energies and second the Higgs-strahlung process $e^+e^- \to ZH^0$ that is dominant for low energies. The corresponding Feynmann diagrams are depicted in Figure 1.1. The WW fusion cross section rises with the CMS energy $\sqrt{s}$ as $log(s/M_H^2)$ and, according to [4], it is given by

$$\sigma(e^+e^- \to W^*W^* \to \nu_e\overline{\nu}_e H) = \frac{g_{WWH}^2}{4\pi}\frac{G_F^2}{8\pi^2}\Big[\Big(1+\frac{M_H^2}{s}\Big)\log\frac{s}{M_H^2} - 2\Big(1-\frac{M_H^2}{s}\Big)\Big] \tag{1.2}$$

while the cross section for the Higgs-strahlung process scales as $1/s$ and according to [5] it can be written as

$$\sigma(e^+e^- \to ZH^0) = \frac{g_{ZZH}^2}{4\pi}\frac{G_F(v_e^2a_e^2)}{96\sqrt{2}s}\beta_{HZ}\frac{\beta_{HZ}^2 + 12M_Z^2/s}{(1-M_Z^2/s)^2} \tag{1.3}$$

with $a_e = -1$, $v_e = -1 + 4\sin(\theta_W)^2$ and $\beta_{ij} = [1-(M_i+M_j)^2/s][1-(M_i - M_j)^2/s]$.

There is also another process that contributes to the Higgs production, the ZZ fusion mechanism. The cross section of the reaction $e^+e^- \to Z^*Z^*e^+e^- \to e^+e^-H$ is strongly suppressed compared to WW fusion.

Having fixed the Higgs boson mass the branching ratios for Higgs decays are completely determined. The most dominant decay is $H_0 \to f\overline{f}$ for $M_Z \leq M_H \leq$

140 GeV with partial decay width given by

$$\Gamma(H_0 \to f\overline{f}) = \frac{g_{ffH}^2 M_H^2}{4\pi} \frac{N_C}{2} M_H \Big(1 - \frac{4m_f^2}{M_H^2}\Big)^{\frac{3}{2}} \tag{1.4}$$

with $N_C = 1, 3$ for leptons, quarks respectively. Decays into ZZ and WW channels are significantly dominant above the 140 GeV threshold. The partial decay width can be expressed as

$$\Gamma(H^0 \to VV) = \frac{g_{VVH}^2}{4\pi} \frac{3\delta_V}{8M_H} \Big(1 - \frac{M_H^2}{3M_V^2} + \frac{M_H^4}{12M_V^4}\Big) \Big(1 - \frac{4M_V^2}{M_H^2}\Big)^{\frac{1}{2}} \tag{1.5}$$

with $\delta_W = 2$ and $\delta_Z = 1$.

The total decay width of the Higgs boson is obtained by adding up all remaining decay channels. For the top quark mass $m_t = 175$ GeV and $M_H \leq 140$ GeV its typical value is less then 10 MeV but with increasing the Higgs mass the width spreads up to 1 GeV.

Precise measurement of the SM Higgs boson mass M_H can be best performed by exploiting the kinematics of the Higgs-strahlung process $e^+e^- \to Z^* \to ZH^0$. Supposing the SM couplings the neutral Higgs particle decays predominantly into $b\overline{b}$ pair. Depending on the leptonic or hadronic decay mode of the Z boson the H^0 boson is either reconstructed from the $b\overline{b}q\overline{q}$ four-jet final state or from the $b\overline{b}l^+l^-$ dijet and lepton pair final state. The measurement of the production cross section for the WW fusion and for the Higgs-strahlung probes the Higgs couplings g_{HWW} and g_{HZZ} respectively. The cross section can be determined independently of the H^0 decay modes by analyzing the mass spectrum of the system that recoils from the Z boson. The total decay width of the Higgs boson Γ_H can be obtained directly for $M_H \geq 200$ GeV. For lower values of the Higgs mass (below the ZZ threshold) Γ_H is extremely narrow and a semi-direct method based on combination of measuring the coupling constants with corresponding branching ratios is used to determine the total decay width.

1.2.2 Physics Beyond Standard Model

As energies are increased some new physics emerging beyond the SM may occur. The alternative scenarios range from supersymmetric theories that incorporate the lightest Higgs particle to completely different alternatives omitting the Higgs mechanism and involving the electroweak symmetry breaking via new strong interactions.

Supersymmetry

One of the most attractive extension of the SM is introducing supersymmetry (SUSY) which is the only non-trivial extension of the Poincare group in quantum field theory. SUSY incorporates gravity and it is also included in the superstring theory. As a desired result a fundamental theory of all basic interactions in nature might be obtained.

SUSY suggest assigning fermions and bosons to common multiplets which brings a possible solution to the hierarchy problem. The radiative corrections to the electroweak intermediate bosons masses include quadratically divergent terms which are canceled in natural way by introducing fermion-boson symmetry. A divergent bosonic loop is added up to a fermionic loop of opposite sign.

In the baseline context of the SM one is left with one doublet of the Higgs scalar field. The supersymmetric extensions require introducing more Higgs doublets or singlets. The simplest option, called the minimal supersymmetric extension of the standard model (MSSM), demands two Higgs field doublets to break the electroweak symmetry. In such a case the Higgs spectrum contains five physical states: two CP-even bosons h^0, H^0, a CP-odd boson A^0 and two charged particles $H^{\pm}$. Except the extended Higgs sector the MSSM contains also supersymmetric partners of the SM particles: sleptons, squarks and gauginos. The MSSM can predict the measured value of $sin^2\,\Theta_W$ with high accuracy and allows the unification of the gauge couplings of strong and electroweak interactions. Hence the MSSM incorporates the electroweak symmetry breakdown in a very natural way.

Imposing SUSY overlaps the ridiculous gap between the electroweak scale and the GUT scale (or Plank scale) and it is favorable especially due to the successful prediction of the electroweak mixing angle. However, there exist theories that solve the hierarchy problem in radically different way.

Alternative Theories

The Higgs mechanism of electroweak intermediate bosons mass generation can be bypassed by introducing new strong interactions at the TeV scale. The global symmetry breaking is associated to the process where the masses of the gauge fields are generated. In the past the strong interactions led to discovery of an internal structure of interacting particles. From this point of view the point-like structure of leptons, quarks and calibration bosons might be impugnable. Another theory providing an alternative to the SUSY consist in extending the Minkowski-Einstein spacetime by extra space dimensions. The gravity is suggested to be strong already at the TeV scale in the new space and the hierarchy problem is completely ruled out.

1.2.3 Cosmology

It is generally supposed that after the Bing Bang the cooling and expansion of the universe was driven by one universal force which split up into three distinct forces. Therefore the proper understanding of the unification of the electromagnetic, weak and strong force might shed light on the development of our universe in the first seconds of its existence.

Measurements of the cosmic microwave background brings the following picture of the universe: only about 4% of the matter corresponds to stars and

interstellar gas, another 23% is so called dark matter which existence is deduced from the motion of celestial bodies, the origin of remaining 73% of the universe's matter still defy conventional explanation. One of the most favored canditate for the dark matter is the lightest supersymmetric particle.

1.3 Parameters and Construction of ILC

A brief overview of the ILC baseline design is given in the following section. More detailed information can be found in [6].

In order to meet the physical requirements mentioned in Section 1.2 the ILC is expected to attain a peak luminosity of 2×10^{34} at CMS energy of 500 GeV. Hence the machine must be designed to be upgradeable to a CMS energy of $\sim$ 1 TeV in the future. Taking into account a collider availability of 75% the integrated luminosity of 500 fb^{-1} can be obtained in the first four years of the physics operation. The power consumption necessary for achieving the proposed peak luminosity is $\sim$ 230 MW. The accelerator is based on superconducting technology operating at radio freqency (RF) of 1.3 GHz and achieving the accelerating gradient of 31.5 MV/m. The total site length necessary for reaching the demanded 500 GeV CMS energy is 31 km and the length must be significantly increased for a possible upgrade to 1 TeV.

1.3.1 Accelerating Technology

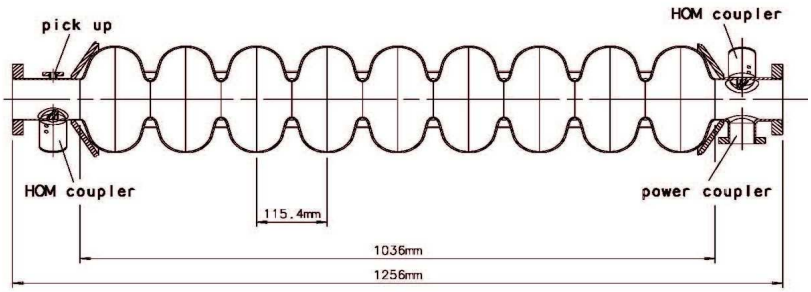

Figure 1.2: Side view of the 9-cell niobium superconductive cavity. The main power coupler port and two higher-order mode (HOM) couplers are depicted [1].

The accelerating structures designed for the ILC are 1 m long 9-cell cavities operating at L-band frequency (f = 1.3 GHz) made of niobium and bath-cooled by superfluid helium to 2 K. The accelerating field is produced with long, low

peak power RF-pulses which is feasible due to small power dissipation in the cavity walls. The relatively small frequency allows achieving a high energy beam power (due to a high RF to beam power transfer efficiency) as well as keeping the beam emittance extremely small. The longitudinal wakefield scales as f^2 while the transverse one as f^3. Therefore machines operating at S-band or X-band region (with frequencies 3 GHz and 11.4 GHz respectively) require higher wakefields compared to that for the ILC. A single cavity is $\sim$ 1 m long and achieves the accelerating gradient of 35 MV/m. The cavity quality factor Q_0 related to the demanded cooling power is typically $\sim 10^{10}$. A low-temperature cryomodule houses a string of eight cavities. Figure 1.2 shows schematic view of the superconductive wave structure.

1.3.2 General Layout of ILC

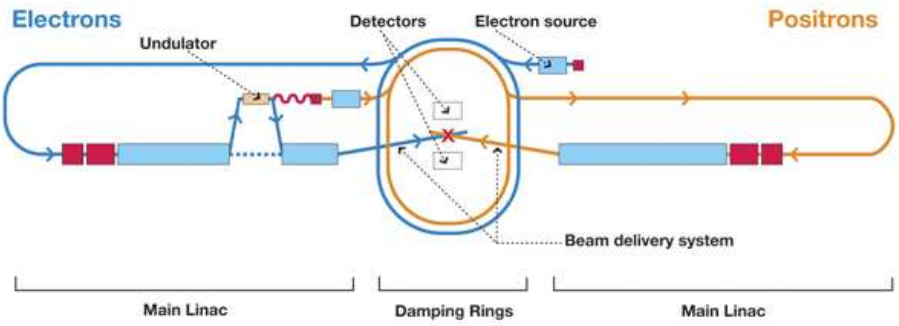

Figure 1.3: Sketch of the overall layout of ILC [10].

The baseline version of the ILC is designed for head-on collision of electron and positron beams with maximum CMS energy of 500 GeV. The general layout consisting of two main linacs, dumping rings, particle sources and injection systems is depicted in Figure 1.3. Table 1.1 presents the overall collider parameters.

Particle Sources

The electron source is optimized for the production of polarized electron bunches (polarization higher than 80%). The production mechanism is based on illu-

CMS Energy	[GeV]	500
Peak Luminosity	$[\mathrm{cm}^{-2}\mathrm{s}^{-1}]$	2×10^{34}
Repetition Rate	[Hz]	5
Total Site Length	[km]	31
Total AC power consumption	[MW]	230
Main Linacs:		
Accelerating Gradient	[MV/m]	31.5
Length of Each Linac	[km]	11
Beam Pulse Length	[ms]	1
Beam Current	[mA]	9.0
Dumping Rings:		
Beam Energy	[GeV]	5
Circumference	[km]	6.7

Table 1.1: Basic design parameters for the ILC [6].

minating a photocatode in a DC gun by a high intesity laser. The beam is preaccelerated to 76 MeV using conventional normal conducting technology. A superconducting linac accelerates the beam to 5 GeV before entering the dumping ring.

The positron injection system is demanded to provide a total charge of $\sim 5 \times 10^{13}$ e^+ per beam pulse. The positrons are produced in high energy photon conversion into e^-e^+ pair on a thin target ($0.4X_0$ titanium alloy). The photons are generated in a 150 m long helical undulator. The 150 GeV electron beam is deflected from the beamline of the main linac and after passing the undulator it is returned back. This configuration effects the electron beam by increasing the energy spread from 0.5×10^{-3} to 1.5×10^{-3} and involves the energy loss of $\sim$ 3 GeV. Therefore additional RF units are necessary for the electron linac to compensate the lost energy. The conventional way of positron production, e.g. electron scattering on a thick target, is deficient for achieving sufficiently high positron beam intensity. Hence the positron beam generated with use of thin target has smaller size and smaller transverse emittance compared to the conventional thick target production. The positrons created in the photoproduction pass through an optical device that matches them into a normal conducting capture system. At this stage the positron beam is accelerated to 125 MeV and the remaining photons and electrons are dumped. The positron beam is then preaccelerated to 400 MeV by means of a normal conducting linac. The dumping ring operates at beam energy of 5 GeV which is reached by a superconducting booster linac. The beam has polarization of 30% with possible upgrade to 60%.

Damping Rings

The e^+ and e^- beams are encumbered with large longitudinal and transverse emittance which is insufficient for achieving the required luminosity. The dump-

ing rings (DR) operating at a beam energy of 5 GeV are designed to reduce the emittances significantly within the 200 ms between machine pulses. Another task is to damp incoming beam jitter in order to provide stable beams for the main linac. Feed-forward systems compensating for pulse-to-pulse variations in the beam charge (and other parameters) require the DR to delay incoming bunches. Hence the emittance and stability of the stored bunches must not be affected by the injection or extraction.

There are two DR, one for electrons and one for positrons, located in the central area of the ILC complex. Both rings are housed in a common tunnel that lies 10 m above the beam delivery system. The dumping ring circumference of the total length of 6.7 km is divided into six straight sections and six arcs. Two straight sections are equipped with the extraction and injection systems while the remaining four contain the superconducting wigglers. The wigglers have total length $\sim$ 200 m per each DR and are operated at temperature of 4.5 K with a magnetic field of 1.67 T. The superconducting RF frequency is chosen to be half the main linac frequency (i.e. 650 MHz) which allows to accommodate varying beam patterns.

The DR should cope with several problems like the electron cloud effect, the fast ion instability and demand for very fast rise and fall time kickers.

Main Linacs

The ring to main linac (RTML) is responsible for transport of the electron and positron beams to the upstream ends of their respective linacs from the DR located at the center of the ILC complex. The beam passes through a 13200 m long 5 GeV transportline where betatron and energy collimation systems are located in order to cope with the beam halo generated in the DR. The transport line is followed by a a 218 m long 180 turn around. The beam is focused into a spin rotator that allows to orient the beam polarization to any arbitrary angle. Since the bunch length in the DR is insufficiently high compared to that required at the interaction point the RTML must perform the bunch compression from 9 mm to a few hundred microns. The system of bunch compressors inserted downstream after the spin rotator also performs 5 to 15 GeV acceleration of the beam (this is necessary in order to reduce spread of energy connected with the bunch compression).

The main linacs are housed in an underground tunnel of 4.5 m interior diameter accompanied with a parallel service tunnel of the same diameter. Except the large experimental hall housing the detector other seven additional surface halls are located in 5 km intervals along both linacs. These halls contain cryogenetic plants, each with installed equivalent cooling power of 20 kW at 4.5 K, servicing the main linacs and the RTLM.

The main linac accelerates the beam from 15 to maximum 250 GeV over a length of 11 km. The beam delivery system requires the two main linacs to make an angle of 14 mrad. Within the ILC physics programme collision energies in range from 50 to 250 GeV are demanded. At the beam point of the electron linac where the electron energy reaches 150 GeV the positron production system

is installed increasing thus the total length of the machine by 1.2 km. If energies lower than 150 GeV are demanded the electron beam will be decelerated after passing the positron production system.

The basic components of the linacs are RF units. A single RF unit consist of RF source that supply three cryomodules. 9, 8 and 9 superconductive cavities are contained in each cryomodule respectively. The RF source is equipped with a 10 MW multi-beam klystron and a RF waveguide distribution system that powers the individual cavities. The high-voltage pulse is generated in a conventional pulse-transformer type modulator (120 kV, 140 A) placed closely to the klystron. The total number of the RF units is 278 for the positron linac and 282 for the electron linac. The RF source including the modulator and the klystron is located in the parallel service tunnel being connected to the cryomodules in the accelerator tunnel via narrow penetration protecting thus the device from radiation exposure and making the maintenance easier.

Beam Delivery System

The main task for the beam delivery system (BDS) is to transport the e^+e^- beams from the downstream ends of the main linacs to the interaction point, bring them to the head-on collision and transport the spent beams to the beam dumps. The baseline design of the BDS is optimized for collisions at CMS energy of 500 GeV while the possible upgrade to 1 TeV requires additional magnets. The overall length of the BDS is 4.5 km both for the electron and positron beams. For the physics experimentation two detectors are designed to share the common interaction region in a push-pull configuration, i.e. a detector that is not currently in use is shifted away from the IR and replaced by the other one. A former configuration encountered two distinct collision points with the both detectors having a fixed position.

The main subsystems of the BDS that perform the demanded functions are the diagnostic region, the fast extraction beamline, the betatron and energy collimation region, the final focus region, the interaction region and the extraction line.

The diagnostic region includes instruments for monitoring the key physics parameters like emittance, energy and polarization and it also includes a collimation system protecting the downstream components. If the beam is not needed at the IP or missteered beams occur the fast extraction beamline is used to extract and dump the beam. The betatron and energy collimation region contains collimators that remove large amplitude particles (beam halo) and it is also equipped with magnetized iron shielding that deflects muons away from the detector. In the final focus region the beam sizes are reduced to the values imposed by the ILC luminosity goals. Demagnifying of the beam is performed by superconducting quadrupoles. The interaction region contains final focus quadrupoles that are integrated into the detector. In order to reduce the influence of the detector solenoid field on the colliding beams additional optical elements are implemented in this region. The extraction line transports the disrupted beam into the water-cooled dump that, beside the the charged par-

ticles, absorbs also the most of the beamstrahlung photons. Before dumping the beam the post-collision polarization and energy diagnostics is performed. Since the main linacs are oriented at the 14 mrad angle the BDS includes crab cavities in order to rotate the bunches horizontally for the head-on collision. The advantage of the 14 mrad geometry is obtaining space for the extraction lines.

1.3.3 Beam Parameters

A set of beam parameters that corresponds to the designed luminosity of 2×10^{34} cm^{-2}s^{-1} at 500 GeV is not unique. Experience with previous accelerators showed that achieving the proposed luminosity with a single set of parameters brings unanticipated difficulties. The ILC can be operated with a wider range of the basic beam parameters. Each parameter set delivers the same luminosity but the option of tuning the specific beam parameters allows to cope with problems such as the kink instability in the final focus system, emittance preservation or beam instability in the damping rings.

The nominal set of parameters for the baseline design is broadened with three different sets: Low P (low beam power), Large Y (large vertical emittance) and Low N (low number of particles per bunch). Lowering the beam power might be imposed by limitations in dumping rings, main linacs, beam delivery system or injection systems. The parameter set with the beam current reduced by 30% and the beam power reduced twice causes the beamstrahlung to increase roughly by a factor of two. Tuning difficulties in the beam delivery system or dumping rings might preclude achieving the proposed normalized RMS veritical emmitance of 0.04 mm·mrad. The increased beamstrahlung caused by the large vertical emittance is reduced by using a longer bunch which gives rise to the disruption parameter at the IP. Reducing the bunch population of 2×10^{10} by a factor of two is beneficial when coping with difficulties such as a large disruption parameter at the IP, microwave instabilities in the dumping rings or a single bunch wakefield emittance dilutions. Any of the three diversions from the nominal set of parameters reduces the luminosity which must be compensated by tighter focusing at the IP. The set of the nominal parameters togeather with the alternative sets is presented in Table 1.2.

The CMS energy of the collision must be supplemented with the sufficiently high luminosity L which requires very high beam powers and extremely small spot sizes at the interaction point (IP). According to [7] the quantitative expression of the luminosity reads

$$L = \frac{P_b}{E_{CMS}} \times \frac{N}{4\pi\sigma_x^*\sigma_y^*} \times H_D \tag{1.6}$$

with E_{CMS} being the collision central mass energy, N number of electrons(positrons) per bunch, $\sigma_{x,y}^*$ the beam size at the IP and H_D the luminosity enhancement factor. The H_D is defined as a ratio of the effective luminosity over the geometrical one with typical value $H_D \approx 1.5$. P_b stands for the average beam power

		Nominal	Low P	Large Y	Low N
Repetition frequency	f_{rep} [Hz]	5	5	5	5
Number of particles per bunch	N [10^{10}]	2	2	2	1
Number of bunches per pulse	n_b	2625	1320	2625	5120
Bunch interval in the main linac	t_b [ns]	369.2	480	369.2	189.2
Average current in the main linac	I [mA]	9.0	6.8	9.0	9.0
Normalized emittance at IP	$\gamma\epsilon_x^*$ [mm.rad]	10	10	12	10
Normalized emittance at IP	$\gamma\epsilon_y^*$ [mm.rad]	0.04	0.035	0.08	0.03
Beta function at IP	β_x^* [mm]	20	11	11	11
Beta function at IP	β_y^* [mm]	0.4	0.2	0.6	0.2
RMS beam size at IP	σ_x^* [nm]	639	474	474	474
RMS beam size at IP	σ_y^* [nm]	5.7	3.8	9.9	3.5
RMS bunch length	σ_z^* [μm]	300	200	500	200
Disruption parameter	D_x	0.17	0.21	0.52	0.11
Disruption parameter	D_y	19.4	26.1	24.9	14.6
Beamstrahlung parameter	Υ	0.048	0.097	0.038	0.050
Beamstrahlung energy loss	δ_E	0.024	0.055	0.027	0.017
Luminosity enhancement factor	H_D	1.71	1.64	2.18	1.48
Geometrical luminosity	L_G [$10^{34}\mathrm{cm}^{-2}\mathrm{s}^{-1}$]	1.20	1.21	0.94	1.35
Luminosity	L [$10^{34}\mathrm{cm}^{-2}\mathrm{s}^{-1}$]	2	2	2	2

Table 1.2: The nominal and designed range of the beam parameters for the ILC [6].

introduced as $P_b = E_{CMS} n_b N f_{rep}$ where n_b is the number of bunches per pulse and f_{rep} is the pulse repetition frequency.

The effect of the beamstrahlung (hard synchrotron radiation emitted during head on collision of opposite charged bunches) plays important role at collision energies in question. In order to reduce the undesirable experimental background and a spread of collision energy the beamstrahlung energy loss δ_E has to be kept at level of few percent. The formula for the average fractional beam energy loss reads [8]

$$\delta_E \approx 0.86 \frac{r_e^3 N^2 \gamma}{\sigma_z^* (\sigma_x^* + \sigma_y^*)^2} \tag{1.7}$$

with r_e being the classical electron radius and γ the relativistic factor E_{beam}/m_0c^2. The luminosity can be increased by lowering the vertical beam size σ_y^* that is expressed by means of normalized vertical emittance ϵ_y^* and vertical beta function at the IP β_y^* as $\sigma_y^* = \sqrt{\epsilon_y^* \beta_y^* / \gamma}$. The bunch length gives the lower bound on the vertical beta function ($\beta_y^* = \sigma_z^*$) thus the luminosity can be recast as

$$L \approx 5.74 \cdot 10^{20} m^{-3/2} \times \frac{P_b}{E_{CMS}} \times \sqrt{\frac{\delta_E}{\epsilon_y^*}} \times H_D \tag{1.8}$$

Decreasing the vertical emittance can be achieved by reducing the bunch charge, reducing the repetition rate, making use of the beam-based correction and alignment and reducing the bunch length. The benefits of keeping ϵ_y^* parameter as small as possible are higher luminosity, reduced beamstrahlung and lower AC-power.

Varying the beam parameters is not entirely arbitrary since the parameters are correlated. For instance, the option with the low bunch population requires the highest number of bunches per pulse with the shortest bunch length. Tuning values of the beam parameters introduces a subject for the future extensive study.

1.4 Complementarity of ILC and LHC

The LHC and the ILC represent different ways of reaching higher energy scales. The LHC programme is based on approaching center-of-mass energy as high as possible which is favored for revealing new particles like the Higgs boson or supersymmetric particles. On the other hand precision measurements (masses, couplings, quantum numbers) are strongly complicated since the colliding protons have composite quark-gluon structure. The ILC offers much more clean identification of the new final states combined with large statistics coming from the high luminosity.

The LHC operates at $\sqrt{s} = 14$ TeV. In the proton-proton collision the Higgs boson is produced dominantly via loop induced gluon-gluon fusion but there are also other relevant contributions: WH, ZH, $t\bar{t}H$ and WW/ZZ fusions. The lightest Higgs boson h^0, as predicted by the MSSM, can be discovered in cascade decays of SUSY particles but it can be also observed in SM-like decay modes. In this case the h^0 can be distinguished from the SM H^0 boson through determination of its couplings which is possible only at the ILC.

Supersymmetry should be discovered at the LHC if it is realized at low energies. Strong interacting squarks and gluinos are expected to be produced with large statistics and they can be easily extracted [9]. Charginos, neutralinos and sleptons are produced in complicated cascade decays of squarks and gluinos thus it is extremely difficult to separate the many SUSY processes. Predictions based on model assumptions have to be compared to the experimental distributions revealing thus enough kinematical constrains. The masses of primary and daughter particles can be determined.

Although the ILC doesn't have as large discovery potential as the LHC it offers precise measurements of the SUSY particle spectrum. Masses of SUSY particles are determined with high accuracy which improves the quality of the derivation of the multiple decay chains at the LHC. Precise determination of the couplings, branching ratios, decay widths, mixing parameters in the chargino-neutralino sectors, spin and quantum numbers and other important parameters is achievable only at the ILC. Such measurements should reveal the detailed structure of underlying supersymmetry theory.

Chapter 2

Detector Concept

This chapter gives a brief overview of components of the foreseen ILC detector and mentions issues such as the detector performance and the particle flow approach. The topics presented here are based on [11] and [12].

The complexity of the physics programme for the ILC discussed in previous chapter brings pressure on detector performance. Requirements on track momentum resolution, vertexing, energy flow and hermeticity significantly dwarf those compared to the earlier LEP or SLC. These requirements are also imposed by entirely new approach, called the particle flow approach (PFA), whereas the complete reconstruction of the four-momenta of the all visible particles in an event is needed. This concept relays especially on perfect tracking and a high granularity calorimeter.

2.1 Detector Design Concepts

Concept	GLD	LDC	SiD	4th
Tracking	TPC/Si	TPC/Si	Si	TPC or drift
B-field [T]	3	4	5	3.5
Radius [m]	7.20	6.00	6.45	5.50

Table 2.1: Basic parameters for various detector concepts. Tracking technologies, strength of the magnetic field and the total outer radius of detectors are presented [13].

There exist four different concepts of the detector design that can meet requirements imposed by the PFA. All of them have similar geometrical arrangement, i.e. they consist of an inner vertex detector, a tracking system, a high resolution calorimeter, a muon system and forward calorimetry and tracking systems. The individual concepts differ mainly in detection technologies of their subsystems and in dimensions dictated by strength of the magnetic field. The four concepts are:

- Silicon detector (SiD) concept [14] relays on an integrated tracking system that, as seen from the interaction point (IP), consists of a pixelated vertex detector and a central microstrip silicon tracker. Tracking information is completed and precised due to a pixelated silicon electromagnetic calorimeter with tungsten as an absorber. A multilayer hadronic calorimeter with high segmentation introduces, together with the electromagnetic calorimeter, powerful tool for the particle flow reconstruction. A muon system is considered with strip-scintillator detectors and resistive plate chambers (RPCs).

- Gaseous large detector (GLD) concept is based on a large volume gaseous central tracker for which serves a TPC. An electromagnetic calorimeter has fine segmentation with a tungsten-scintillator structure while a hadronic calorimeter employs a lead-scintillator structure. More details can be found in [15].

- Large detector concept (LDC) involves a tracking system based on a large volume time projection chamber (TPC) completed with a high precision silicon-strip vertex detector. Calorimetry is based on a high granularity electromagnetic calorimeter with tungsten absorbers and silicon detectors. A hadronic calorimeter is foreseen either with scintillation based particle detection or gas chambers. A tough muon system surrounds a large superconducting coil and covers almost the whole solid angle.

- The fourth detector concept employs the same vertex detector as the SiD design and the TPC is similar to those for the LDC and GLD. A novel outer muon system and a double-fiber readout calorimeter with fine segmentation are under study [16].

Table 2.1 summarizes the basic parameters of different detector concepts. This thesis is deticated to the measurements connected with the scintillator tile hadronic calorimeter therefore only the LDC is discussed in what follows.

2.2 Detector Components

Figure 2.1 shows the general layout of the basic components of the ILC detector. Its total outer radius is 6 m and length 12.4 m. The interaction point (IP) is closely surrounded with a pixel vertex detector (VTX) of minimum material thickness and excellent point resolution. The large volume time projection chamber (TPC) allows excellent 3D point resolution. The gap between the TPC and the VTX is bridged with additional Si pixel and strip detectors. The forward direction is covered by a system of Si discs. A granular electromagnetic calorimeter (ECAL) surrounding the TPC has a transverse segmentation 1×1 cm^2 and 30 layers radially. Behind the ECAL a granular scintillator based hadronic calorimeter (HCAL) is located. Both calorimetric and tracking systems lie inside a large volume superconducting coil that provides a longitudinal magnetic field of nominal value 4 T. A large barrel yoke with two endcaps encapsulates the whole detector volume. The iron yoke is instrumented with layers of tracking detectors since it fills two tasks: first it returns the magnetic flux of the magnet and second it serves as a muon detector and filter. Since there is no external trigger a sophisticated data acquisition system is necessary in order to monitor the electron-positron collisions. Additional calorimeters placed in very forward region monitor the quality of the collision and measure the luminosity. The individual detector components are described in more detail in the following sections.

2.2.1 Tracking Systems

The track momentum resolution should reach $\Delta(1/p) = 5 \times 10^{-5}$ GeV^{-1} in the central region in order to achieve the optimal precision in the determination of the recoil masses, e.g. for reactions such as $Z \to ll$. The high momentum resolution is demanded also in the forward region together with a very good angular

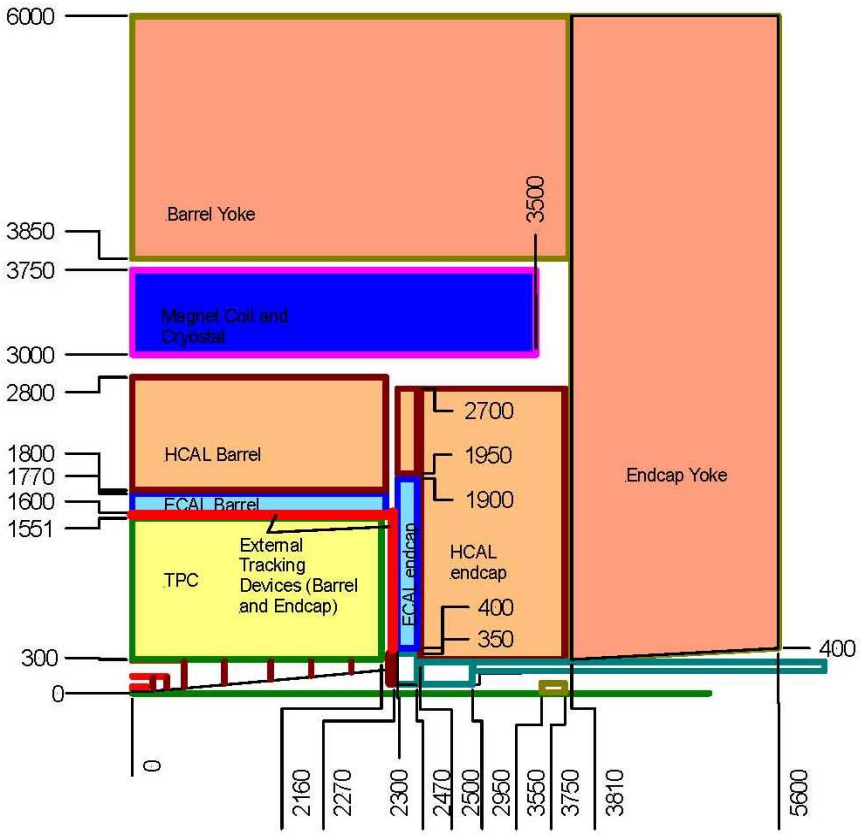

Figure 2.1: Sketch of one quarter of the proposed ILC detector design, dimensions are in mm. The detailed view of the tracking system is depicted in Figure 2.2. [11]

resolution which allows to measure the luminosity spectrum with Bhabha events (electron-positron elastic scattering). Very high capabilities of the c and b quark tagging are imposed by identification of the multi-b final states (ZZH, $t\bar{t}H$) and by distinguishing between $H \to c\bar{c}$, $H \to b\bar{b}$ decays. Since the high-energy jets have very high local track density the responsible pattern recognition capability is necessary.

The tracking detectors can be divided into three groups (See Figure 2.2):

- Vertex detector
- Central tracking detectors
- Intermediate tracking system

VTX	Radius		Half-length in z
Layer 1	16		50
Layer 2	26		75
Layer 3	37		75
Layer 4	48		75
Layer 5	60		75
SIT	Radius		Half-length in z
Layer 1	150		180
Layer 2	290		450
FTD	Inner Radius	Outer Radius	Half-length in z
Disc 1	40	138	180
Disc 2	47.5	140	300
Disc 3	57.5	280	450
Disc 4	87.5	280	800
Disc 5	122.5	280	1200
Disc 6	157.5	280	1550
Disc 7	187.5	280	1900
Disc 8 (LumiCAL)	92.5	350	2240
TPC	Inner Radius	Outer Radius	Half-length in z
TPC overall	300	1580	2160
Fieldcage inner cyl.	300	350	2000
Fieldcage outer cyl.	1480	1580	2000
Endplate TPC	300	1580	160

Table 2.2: Main parameters of the tracking detectors, dimensions are in mm [11].

The vertex detector (VTX) is a high precision silicon based pixel device consisting of five concentric layers that surround the IP. The vertexing performance is achieved by locating the innermost layer as close as possible to the IP and by a large solenoidal field. The beam-beam interactions produce dominantly the e^+e^- background of density about 0.03 hits mm^{-2} per bunch crossing which is confined radially by the 4 T magnetic field.

The central tracking system relays on a large volume time projection chamber (TPC) and a forward tracking chamber (FCH). The TPC is found to be optimal solution for very high track finding efficiency and track resolution. About 200 points along a track can be measured providing spatial coordinates and information on the energy loss of the traveling particle. Possible ambiguities caused by matching different projections are excluded due to the direct measurement of three-dimensional spatial points. Sufficiently large radius of the TPC allows very good momentum resolution as well as high pattern recognition with large backgrounds or in a dense jet environment. The FCH consist of 6 planes containing straw tubes with 5 mm in diameter.

The intermediate tracking focuses on the space between the VTX and the TPC. Silicon tracking detector (SIT) consist of two cylinders in a barrel and it is based on the strips technology. Eight forward tracking discs (FTD) which

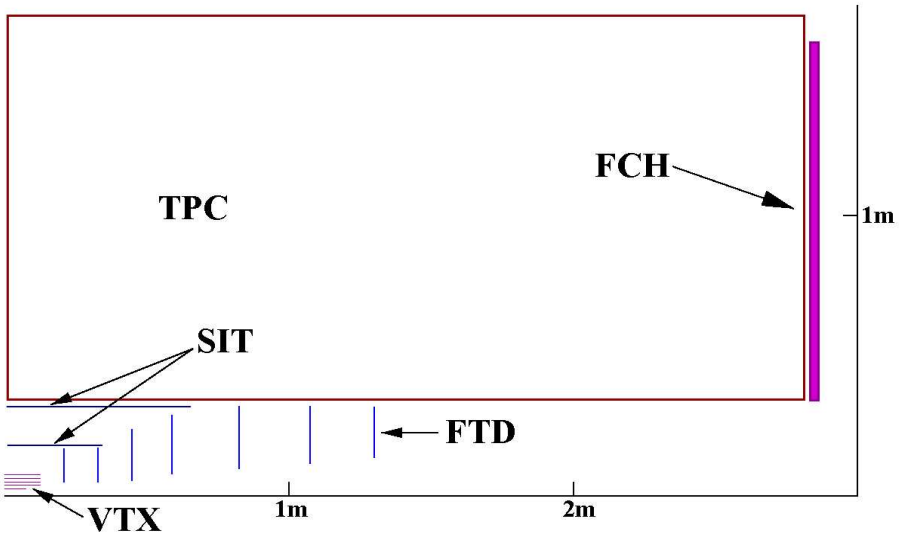

Figure 2.2: Schematic drawing of the tracking system showing one quarter of the proposed design, dimensions are in mm [12].

are designed as planes perpendicular to z axis located along the beam direction serve especially for improvement of the tracking performance since many final states are expected to have jets in either very forward or backward region.

The main parameters of individual tracking subsystems are summarized in Table 2.2.

2.2.2 Calorimeter Systems

	Inner Radius	Outer Radius	Z start	Z end
ECAL:				
Barrel	1600	1770	0	2200
Endcap	400	1800	2300	2470
HCAL:				
Barrel	1800	2900	0	2200
Endcap	300	2800	2500	3800
Ring	1950	2800	2300	2470

Table 2.3: Main parameters of the electromagnetic and hadronic calorimeters, dimensions are in mm [11].

In order to make full use of the high luminosity of the ILC the mass of pairs of hadronic jets is demanded to be measured with the precision of 3%.

This is achiveable within the particle flow approach where all particles in a jet are measured individually. While the contribution from charged particles is measured in the tracking systems dealing with the contribution from photons and neutral hadrons is the key task for the high granularity calorimeter. The excellent energy resolution for jets forces the calorimeter to be as hermetic as possible.

The calorimeter is divided radially into the electromagnetic and hadronic part. The electromagnetic calorimeter (ECAL) is optimized for reconstruction of electrons and photons and their separation from hadronic showers occurring due to charged hadrons interactions in the device. The hadronic calorimeter (HCAL) is designed to measure energy depositions of neutral hadrons in a dense jet environment which requires high precision in separation of nearby hadronic showers. As seen from the interaction point the ECAL is located in front of the HCAL. Both parts of the system are mounted inside the superconducting coil that produces the 4 T magnetic field. This configuration is beneficial since the magnetic field improves the spatial resolution of charged particles and meets the requirement for the hermeticity down to small polar angles. Table 2.3 presents the main parameters of the electromagnetic and hadronic parts of the calorimeter.

Electromagnetic Calorimeter

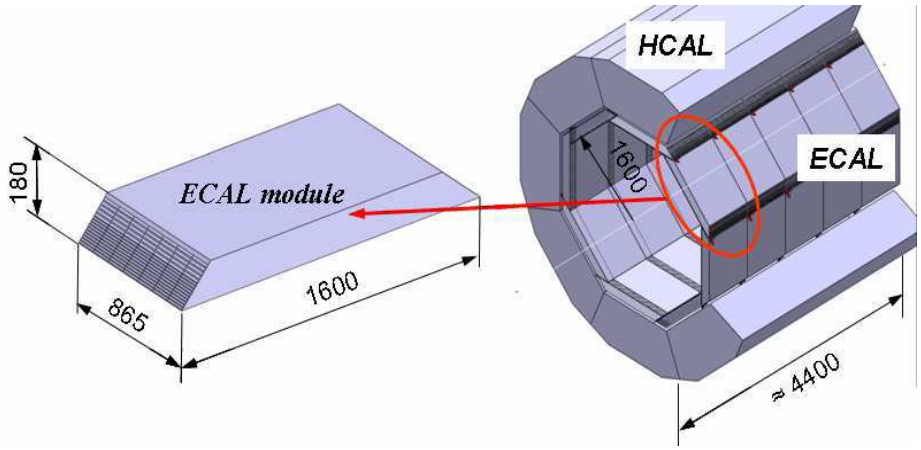

Figure 2.3: The ECAL and HCAL barrel with detailed view of the ECAL module; dimensions are in mm [11].

The electromagnetic calorimeter consists of the octagonal barrel and two endcaps. One eighth of the barrel, so called stave, is divided into five modules along the beam axis. The edges of the modules are skew following the eightfold symmetry so that the cracks contain very large angle with the radial direction. The endcap keeping an octagonal shape is built of four modules with similar

structure and is split vertically into two halves for easy access. There is a 10 cm gap left between the barrel and the endcap; this is necessary to house cables or cooling services. Precise rail systems mount the ECAL to the HCAL stave by stave leaving a gap where cooling, electrical power and signal distributions are placed. The ECAL layout can be seen in Figure 2.3.

The transverse segmentation of the ECAL is considered with 20 layers of tungsten absorber of 0.6 X_0 followed by another 9 tungsten layers of 1.2 X_0 (the radiation length of tungsten $X_0 = 3.5$ mm). Between the tungsten sheets the silicon based active device is inserted.

Isolated electrons coming either from Bhabha events or W,Z electron decays are used to calibrate the overall response of the ECAL. The cosmic muons can be used for intercalibration of the response of the calorimetric cells as well. Both calibration methods achieve the precision at level of few per mille for each cell. Details on the calibration of the ECAL can be found in [17].

The performance of the ECAL was a subject of GEANT 4 based simulations [18]. Although the energy resolution is expected to scale like $\alpha/\sqrt{E}$ the various thickness of the tungsten absorbers yields two distinct regions of the resolution behavior. For lower energies the resolution is found to be $11\%/\sqrt{E}$ while in the region of higher energies the resolution scales as $14\%/\sqrt{E}$. The position resolution is given by mesurement of the angular distribution of photons that originate in the primary interaction point. The resolution of 2 mm can be reached for 1 GeV photons.

Hadronic Calorimeter

Two basic concepts are under study for the hadronic calorimeter within the LDC. First an analogue hadronic calorimeter and second a digital hadronic calorimeter.

The digital HCAL employs detection technology based on gaseous signal amplification which is realized with gaseous electron multipliers (GEMs), micro mesh gaseous structures (Micromegas) or RPCs. Chamber anodes are extremely fine segmented into 1×1 cm^2 pads which allows to obtain the analogue information, necessary for e.g. cluster finding, just by simple counting of hits. Technical description and a summary of the research work can be found in [19]. The following text concentrates on the scintillator tile analogue HCAL (AHCAL).

The AHCAL is a sampling calorimeter with tungsten, steel or brass absorbers. The active medium consists of scintillator plates that are subdivided into tiles. Each tile is read out by a millimeter size silicon photomultiplier (SiPM) thus the front-end electronics is included inside the detector volume in contradiction to the existing calorimeters. The geometrical arrangement of the AHCAL supports the octagonal symmetry of the ECAL: a cylindrical barrel consisting of two parts each subdivided into sixteen modules is covered with endcaps on either side. Each endcap consists of four modules. The AHCAL geometry is depicted in Figure 2.4.

The sampling of the AHCAL is formed by 20 mm (corresponding to 1.15 X_0 or 0.12 λ) absorber plates interleaved with 6.5 mm active scintillator layers.

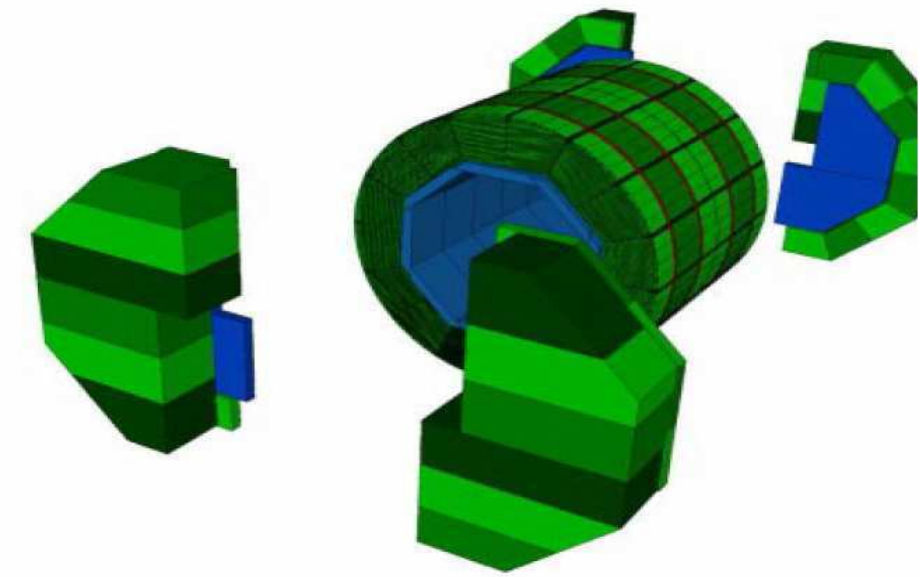

Figure 2.4: The HCAL barrel and the endcaps in the open position [11].

Both the barrel and the endcaps have the same sampling structure with maximum of 38 and 53 layers respectively. The area of the scintillating tiles varies from 5×5 cm^2(the innermost layer) to 25×25 cm^2 (the outermost layer). The tile sizes are suited to a few GeV showers which spread is typically about 20 cm. Note that a physics prototype (PPT) of the AHCAL (discussed in Section 3.1.4) employs different sampling structure with tile sizes in range from 3×3 cm^2 to 12×12 cm^2. The tile sizes for the complete detector might be optimized based on tests performed with the PPT.

All cells of the AHCAL must be permanently calibrated and monitored in order to ensure the sufficient performance of the device. Cosmic muons of momenta higher than 10 GeV/c are favored for the calibration. In order to reach $\approx 3\%$ accuracy about 200 muons per cell are needed. The flux of cosmic muons is high enough to attain the required rate within one week. The endcaps of the AHCAL where the number of penetrating muons is limited can be additionally calibrated by means of muons arising in the beam halo. In order to ensure the stability of the calibration the response of individual cells must be monitored during the operation. A system based on light emmiting diodes (LED) was developed for this purpose (see Section 3.4).

Forward Calorimeters

Covering the forward region is important first to reach the perfect hermeticity of the detector and second to measure the luminosity and the luminosity spectrum. The very forward region is instrumented with two calorimetric devices

(see Figure 2.5):

- the low angle tagger (LAT)
- the luminosity calorimeter (LCAL)

The LAT is designed as a sampling calorimeter with 63 sheets of tungsten (2.6 mm thickness) interleaved with silicon layers (0.5 mm thickness). The segmentation is suggested to have 14 segments radially with the azimuthal segmentation of 15°. The calorimeter provides measurement of electrons extending thus the electromagnetic calorimetry to polar angles below 30 mrad. In addition the LAT works as a shield protecting the tracking system from backscattered particles. The energy resolution was estimated based on simulated response to high energetic electrons with a result of 20-25%/$\sqrt{E}$(GeV).

The LCAL is located in a distance of 220 cm from the IP on both sides of the detector covering the region that extends radially from 1.2 cm to 6.2 cm. The device is capable to measure electron showers serving thus as a luminosity monitor and as a low angle calorimeter. In order to resolve luminosity variations within one bunch train the beam induced background particles must be detected with an accuracy of 1% within small response time (from 30 to 50 ns). The beam delivery system receives information from the LAT in order to tune the beam with respect to the luminosity variations. The LAT is also designed to provide shielding from the synchrotron radiation and from backscattered particles.

2.2.3 Magnet System

The magnet coil together with the cryostat are located behind the HCAL inside the iron yoke of octagonal shape. The yoke is divided into the barrel yoke which extends from 4.45 m to 6.45 m radially with an overall length of 14.8 m and the two octagonal endcap yokes each 3.9 m long. The endcap yokes are divided vertically into to two parts so that the detector is accessible without removing the beamline. The coil extends from 3.16 m to 3.50 m radially with the overall length of 9.2 m and it is divided into five modules longitudinally with 4 layers windings within each module. Since the magnet is foreseen to work at temperature of 4.5 K the coil is embedded in a 10.2 m long cryostat. The windings are supplied with the nominal main current of 18.8 kA providing solenoidal magnetic field of 4 T along the z axis in a volume of 6 m in diameter. The tracking system, especially the TPC demands the magnetic field with very high integral homogeneity

$$\left| \int_0^{2.5} (B_r/B_z) dz \right| \leq 2 \text{ mm} \tag{2.1}$$

where $B_r = B_x(x/r) + B_y y/r$. A relative accuracy of 0.2 % in determination of the B_x, B_y filed components is necessary in order to ensure the required homogeneity. An updated version of the Hall probes that requited when mapping the magnets at ALEPH, DELPHI or H1 is expected to meet this high precission demands. The detailed description of the magnet system can be found in [20].

2.2.4 Muon System

The muon detector should complete two basic tasks: first identification of muons and triggering on them, second catching hadronic showers in order to tag events with a large portion of energy missing in the calorimeters.

The system is located outside the coil and it is segmented in iron slabs used as an absorber. The total length of the barrel is 14.4 m with the inner radius of 380 cm and the outer radius of 580 cm. The end-caps are placed completely inside the barrel and extend radially from 46 cm up to the inner radius of the barrel. The overall thickness is determined by requirements for muon identification performance and the required calorimetric resolution. The thickness of the iron (given by number of slabs) follows the need to contain the magnetic flux (for a 4 T solenoidal field about 1.6 m iron layer is needed). Based on practical reasons the iron slab thickness is suggested to be $\sim$ 10 cm which implies the number of active detector layers is 16 in the barrel and 15 in the end-cap. Reducing the number of the active planes doesn't influence the performance of the calorimetry and the muon identification significantly therefore a more suitable version containing 12 active layers in the barrel and 11 active layers in the end cap is suggested.

The large dimensions of the muon system require inexpensive and very reliable active elements. The choice of the RPCs shows to be the optimal solution. A backup alternative involves plastic streamer tubes but this option brings substantial complication to the detector construction and increases the sensitivity to the background.

2.2.5 Backgrounds and Detector Mask

There are various sources of the beam-induced background originating from hard beamstrahlung photons, synchrotron radiation, beam gas scattering or muons. A detailed discussion on the beam-induced background is presented in [21]. The hard beamstrahlung radiation is responsible for the most significant source of the background; within a single bunch crossing (BX) approximately 6×10^{10} beamstrahlung photons are produced at the CMS energy of $\sqrt{s} = 500$ GeV. Although the photons themselves are lost in the acceptance hole of the detector they cause secondary effects such as e^+e^- pairs, neutrons and other hadrons or radiative Bhabha events. The major background source for the detector comes from the secondary particles that are created when the pair particles hit the quadrupoles of the collimation magnets.

A system of tungsten shielding, called the mask, was designed in order to protect the detector from the background. Figure 2.5 shows the mask geometry. The mask of cylindrical shape surrounds the final quadrupole doublet and it is extended with the conical tip that shields the tracking detectors from the backscattered particles. A tungsten disk forms the inner mask that shields the innermost layer of the vertex detector. In front of the inner mask a layer of graphite that works as a low Z absorber of backscattered showers is inserted. The mask is instrumented with additional devices for beam diagnostic and low

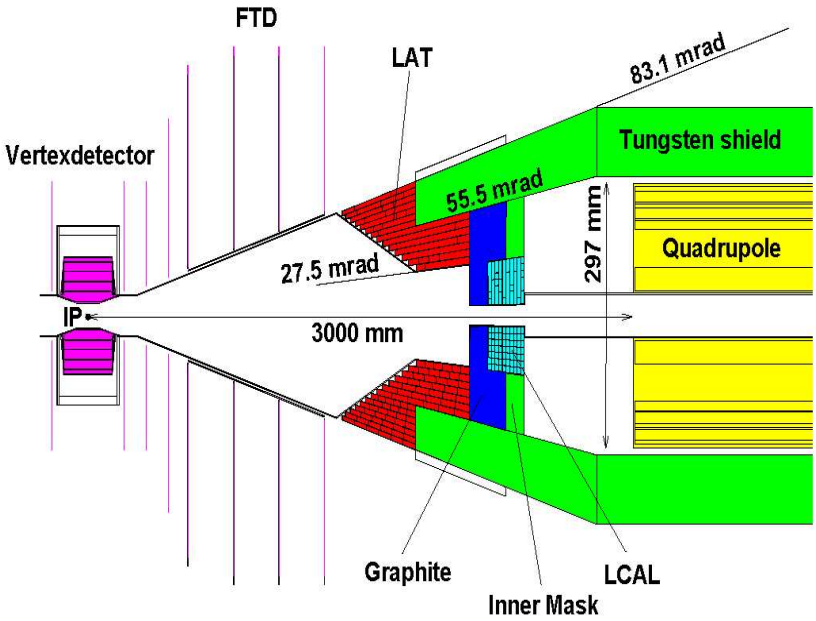

Figure 2.5: The detector mask with the implemented luminosity calorimeter (LCAL) and the low angle tagger (LAT) [12].

angle measurements: the luminosity calorimeter and the low angle tagger. The LCAL is integrated into the inner mask while the LAT is mounted outside the mask. Both the LAT and LCAL are described in Section 2.2.2.

2.3 Data Acquisition

The detector front end has up to 10^9 readout channels with total data volume of 350 MB per train. The data acquisition (DAQ) system should deal with high data stream imposed by the high granularity of the detector and the pulsed operation mode of the ILC machine with 2820 collisions in 1 ms. A period of 199 ms between the bunch trains define the time within the data of the whole detector must be read out. Since there is no hardware trigger the event selection is performed by software.

The network architecture designed for the DAQ system is schematically displayed in Figure 2.6. The readout units (RU) receive the data which are already minimized due to zero suppression and cluster or hit finding performed by individual subdetectors. A single readout unit consists of the interface to the front

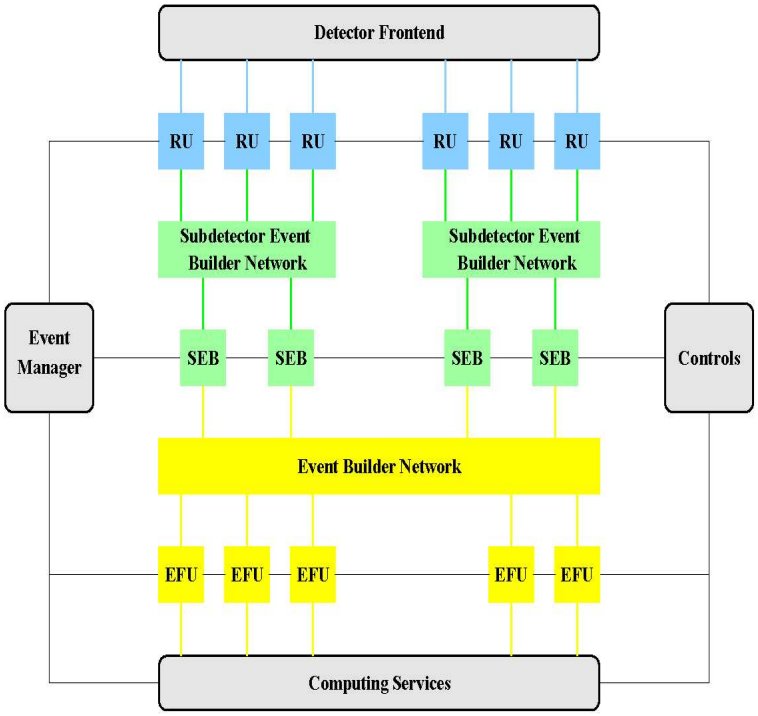

Figure 2.6: Conceptual layout of the proposed DAQ architecture [12].

end readout realized by a fast serial link, the data buffer and the interface to the fast subdetector event building network. The pulse regime of the machine enforces the complete event building to be performed within the period of 200 ms. This a task for event finder units (EFU). Full event reconstruction from the all detector components requires an event building capability of $\sim$ 2 GB/s for a single EFU. Processing a complete bunch train at once demands sufficiently high bandwidth but up to date it is not clear whether this goal is achievable. Therefore an alternative design with parallel event building is considered. The data are preprocessed by subdetector event building units (SEB) where cluster finding or local pattern recognition is performed. The data volume is further sent to the second event building network and then into the final EFUs. Additional buffering is needed to allow to overflow the 200 ms limit.

2.4 Detector Performance

The particle flow approach (PFA) requires to resolve all particles that are visible in an investigated event. Combined information from the calorimetric systems and trackers is necessary to determine four-momenta of all particles contained

	91.2 GeV $Z \to q\overline{q}$	500 GeV $e^+e^- \to t\overline{t}$
σ_ν/GeV	0.84	1.36
σ_{FWD}/GeV	1.55	2.68
σ_{HCAL}/GeV	1.40	3.93
σ_{ECAL}/GeV	0.57	1.40
σ_{mass}/GeV	0.61	1.32
σ_{total}/GeV	2.40	5.31
$\sigma_{total}/\sqrt{E}$GeV	25.1%	23.7%

Table 2.4: Monte Carlo simulation for jet energy resolution contributions for Z events at 91.2 GeV and top pair events at 500 GeV. The presented contributions are: σ_ν assigned to the unobserved neutrinos, σ_{FWD} assigned to the particles disappeared in the forward region,σ_{HCAL} and σ_{ECAL} arise from the HCAL and ECAL respectively [11].

in a jet. About 40% of the jet energy is carried by neutral particles that are mesured with the calorimetric system and the rest by charged particles that are measured with the tracking system. Calorimeter hits must be correctly assigned to the tracks of charged particles which is the crucial task for the particle flow algorithms. These algorithms perform pattern recognition in the calorimeters in order to identify clusters associated with a single particle and to separate nearby showers. Beside the calorimeter reconstruction the tracks of the charged particles are reconstructed as well. The output of the algorithm are so-called particle flow objects (PFO) which are formed by matching the clusters with the reconstructed tracks. Clusters that have no track to be associated with are identified as neutral PFOs corresponding to photons or hadrons. Up to date two types of the particle flow algorithms are under developement: WolfPFA and PandoraPFA. The WolfPFA performs the track reconstruction independently from the calorimeter clustering while the PandoraPFA uses the tracking information to drive the calorimeter hit isolation and forming the clusters. Both algorithms result in into cluster-track matching and the final formation of the PFOs.

The goal for the jet energy resolution is to reach $\Delta E/E = 30\%/\sqrt{E}$ which is a factor two better than the best jet energy resolution at LEP[1] and in addition it is independent from the polar angle due to the fine granularity of the detector. The high energy resolution is motivated by jet-jet invariant mass resolution for $Z \to qq$ and $W \to qq$ decays which is required to be at level of the Z and W natural decay width, e.g. $\sim$2 GeV. The di-jet mass resolution is given roughly as $\Delta m/m = \alpha/\sqrt{E_{jj}}(\text{GeV})$ with E_{jj} being the energy of a di-jet system. Putting in numbers (Δm = 2 GeV and E_{jj} = 150 GeV) one gets a constant for the overall energy resolution $\alpha = 30\%$.

Contributions to the jet energy resolution are given by the resolution of the

[1]The jet energy resolution reached at LEP is$(\Delta E/E = 60\%/[(1 + |\cos\theta|)\sqrt{E}])$

calorimetric systems and the central tracking but the other detector subsystems play role as well. The limited detector acceptance, imprecision of jet-clustering algorithms as well as missing energy from unobserved particles must be also included. Quantitatively the energy resolution can be expressed as

$$\sigma^2 = \sigma^2(X^{\pm}) + \sigma^2(\gamma) + \sigma^2(h^0) + \sigma^2(miss) + \sigma^2(conf) \tag{2.2}$$

with $\sigma^2(X^{\pm})$ being the resolution for charged particles, $\sigma^2(\gamma)$ the resolution for photons, $\sigma^2(h^0)$ the resolution for neutral hadrons, $\sigma^2(miss)$ stands for missing energy coming for undetected particles either lost in the forward region or neutrinos and $\sigma^2(conf)$ stands for the confusion term which concerns possible wrong hits to clusters assignment, imperfection in matching tracks to clusters and imprecision in identification of neutral vertexes. Table 2.4 presents Monte Carlo simulated values of these contributions at energies $\sqrt{s} = 91.2$ GeV ($e^+e^- \to Z \to qq$) and $\sqrt{s} = 500$ GeV ($e^+e^- \to tt$). The confusion term is omitted for this simulation while the effect of some PFOs with wrong assigned mass is encountered in addition.

Another important issue for the detector performance is the flavor tagging capability. Note that the light Higgs boson dominant decay channel is $H \to b\bar{b}$ and the top quark decays dominantly into bW. Thus the multi-b final states like $t\bar{t}H$ or ZHH requires very high efficiency in b-tagging accompanied with a very high suppression of light and c-quarks. On the other hand the measurement of $H \to c\bar{c}$ branching ratio requires a very high suppression of b-quarks and a high c-tagging efficiency. Simulation studies of the b-tagging and c-tagging capability can be found in [22].

Chapter 3

Calorimetry at ILC

The analogue tile hadronic calorimeter (HCAL) design and development is discussed in the following sections. As the particle detection is based on scintillation a novel photo detector, the silicon photomultiplier (SiPM), becomes a favorable photon counting device which, based on successful beam tests, is foreseen to be used in the final calorimeter design. The readout with conventional avalanche photo diodes (APDs) still introduces an open possibility and is a subject of many studies comparing benefits of the both technologies. In addition a versatile monitoring and calibration system is required to ensure the stability of the high granularity complex system.

3.1 Tile Hadronic Calorimeter Structure and Construction

The tile hadronic calorimeter is a sampling device consisting of individual modules that are arranged as a barrel covered with two endcaps. In order to ensure the high quality of the magnetic field iron pole-tips are inserted in the space between the rear of the endcap and the iron return yoke. The pole tips are assembled with scintillator planes and serve thus as a tail catcher in the endcap region. The barrel is divided into two halfbarrels each consisting of 16 modules, a single endcap is built of two modules. Table 3.1 summarizes main parameters of the modules.

HCAL Sections	Barrel	Endcaps	Pole-tips
#Modules	2×16	2×4	2×4
Modules Volume [m^3]	$1.0 \times 1.1 \times 2.74$	$2.9 \times 2.9 \times 1.4$	$2.65 \times 2.65 \times 1.15$
Modules Weight [tons]	15.8	25	65
Polar Angle	90°-35°	35°-4.8°	30°-4.8°

Table 3.1: Structure of the hadronic calorimeter.

3.1.1 Module Structure

Sandwich Structure	Barrel	Endcaps	Pole-tips
Steel/Scint/Fibers [mm]	20/5/1.5	20/5/1.5	400/5/1.5
Depth [cm]	103.8	142	115
Depth [λ]	4.5	8	7
#sandwiches along shower	38	53	3
#individual tile plates	1216	1272	72
#cells along shower	9	12	3

Table 3.2: Sandwich structure for different types of modules.

The HCAL is segmented in depth within 20 mm steel absorber sheets between which 6.5 mm spaces are left. These gaps house the scintillator tiles.

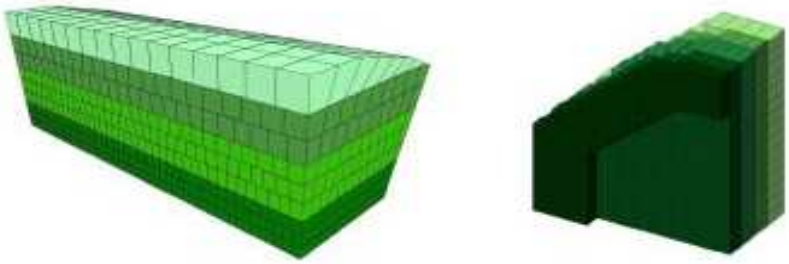

Figure 3.1: The view of the HCAL barrel (left) and endcap (right) module [12].

Although a single tile is 5 mm thick the remaining space of 1.5 mm is necessary for the wavelength shifting (WLS) fiber loop and the reflection layers. Depending from the readout technology the gaps might contain also clear readout fibers and the room tolerance of the fibers and tiles must be accounted as well. The sandwich structure of the modules is entirely held by a 3 mm stainless steel skin which embraces the module from three sides. Figure 3.1 shows the barrel and the endcap module.

The barrel module contains 38 sandwich layers, the endcap module contains 45 sandwich layers and the gap between the endcap and the barrel is filled with 8 additional layers arranged in a ring. One sandwich layer corresponds to 1.15 X_0 or 0.12 λ. Basic parameters of the sandwich structure are presented in Table 3.2. Calorimetric cells are formed by tiles laying in subsequent layers. As seen from the interaction point the number of layers forming a cell varies from 3 tiles at front to 7 tiles at back. The barrel modules are segmented with 9 cell layers in depth. The endcap modules have 10 cell layers with two additional layers corresponding to the outer ring. The scintillating tiles lateral dimensions increase from 5×5 cm^2 in the innermost layer to 25×25 cm^2 in the outermost layer. The cell sandwich structure and the dimensions of cells are summarized in Table 3.3.

3.1.2 Tile-fiber System

The blue light (400-500 nm) produced in scintillators is absorbed with the WLS fiber and emitted as green light. The emission spectrum of the scintillator is shown in Figure 3.3(a). The absorption and emission spectrum of the WLS fiber is depicted in Figure 3.3(b). The WLS fiber has an absorption depth of 600 μm

Barrel			Endcap		
Cells	Sandwiches	Tile size [cm^2]	Cells	Sandwiches	Tile size [cm^2]
			Outer Ring 1	4	13
			Outer Ring 2	4	13
1	3	5×5	1	3	9×9
2	3	5×5	2	3	9×9
3	3	5×5	3	3	9×9
4	4	7×7	4	4	11×11
5	4	8×8	5	4	11×11
6	4	9×9	6	4	11×11
7	5	10×10	7	5	12×12
8	5	12×12	8	5	12×12
9	7	16×16	9	7	21×21
			10	7	21×21
Total	38			45	

Table 3.3: Segmentation of the HCAL barrel and endcap modules [32].

and an absorption efficiency of 70-80%. In order to deliver as much light as possible the downstream end of the WLS fiber is instrumented with a mirror reflector layer. The coupling of the WLS fiber to the scintillating tile can be realized with an optical glue, air gap or one can simply attach the fiber along one side of the tile. The best light yield is obtained when the tiles are instrumented with a machined groove into which the fibers are inserted. The light yield also depends from the length of the fiber inside the scintillation area; various geometrical configurations are depicted in Figure 3.2. Note that although the light yield is an increasing function of the fiber length it saturates if more than two loops are applied. About 10-35% of photons produced in scintillation can be absorbed by the WLS fiber.

The amount of light produced in scintillating tiles must be measured with high efficiency photodetectors. Either the avalanche photo diode (APD) or a novel device, a pixelated silicon photomultiplier (SiPM), are being explored for this purpose (see Section 3.3). The advantage of the SiPMs consists in their small dimensions which allows to mount them directly to the tile. The possibility investigated with APDs was for the light transport realized with long transparent fibers. Up to date double clad fibers of 1 mm diameter with light attenuation length of 12 m (for wavelength of 600 nm) and a bending radius larger than 2 cm are available. This light transport system is foreseen to work with losses smaller than 25%.

3.1.3 Readout Architecture

The HCAL is an analogue device with more than 200 thousand readout channels. The front-end electronics is based on 18-fold multiplexed gain charge preampli-

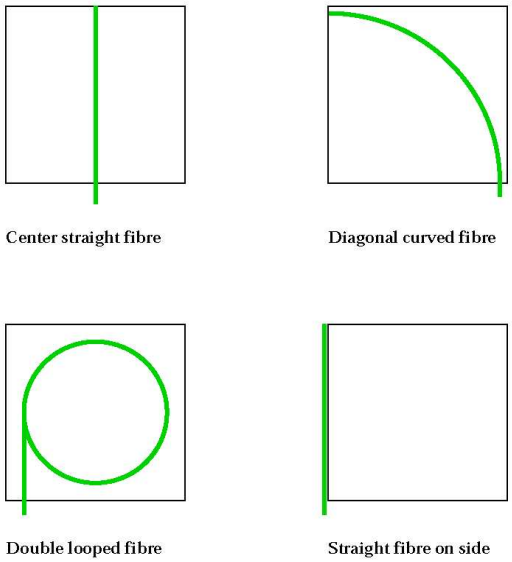

Figure 3.2: Various geometrical arrangements of the WLS fiber to the tile coupling [33].

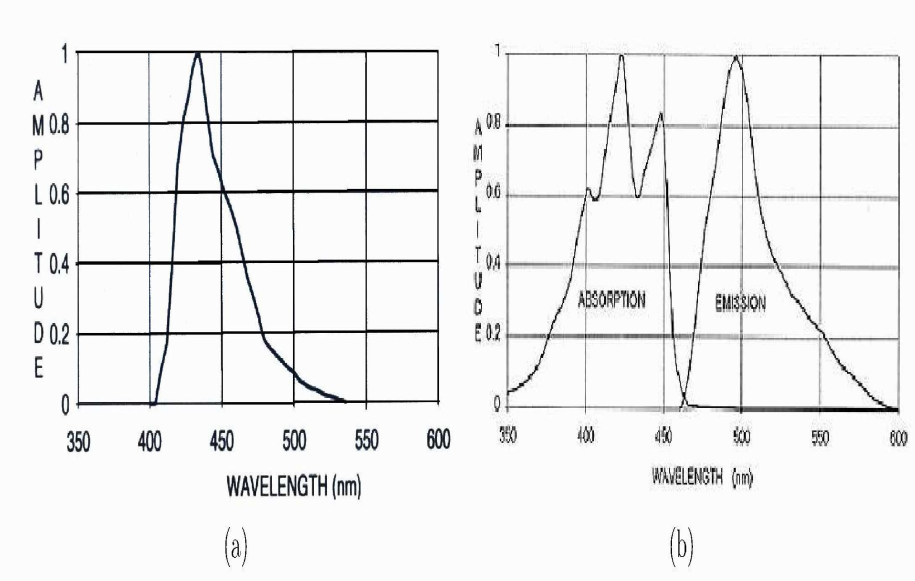

Figure 3.3: (a) The emission spectrum of the scintillator tile with a peak at 430 nm. (b) The absorption and emission spectrum of the WLS fiber. From [31].

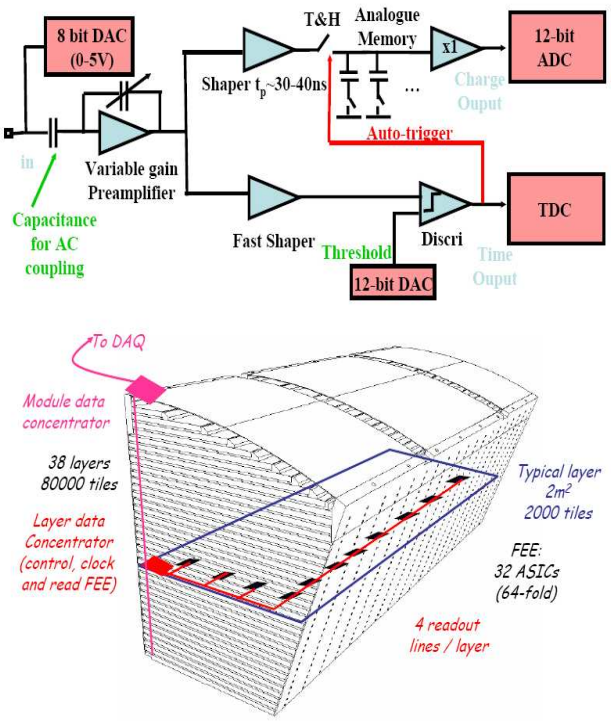

Figure 3.4: The HCAL front end electronics scheme with the ASIC chip containing a variable gain preamplifier and variable shaper leading to the ADC (up) and the readout architecture for a single module with one link to the DAQ (down) [11].

fier followed by a variable shaper with a sample-and-hold in an ASIC chip. All the 18 channels of the ASIC chip are instrumented with 8-bit DACs in order to adjust the SiPM bias voltages. The back-end electronics involves VME CALICE readout cards (CRCs) with 8 input ports, each port reading 12 ASIC chips. The multiplexed signals are converted to the digital form with 12-bit ADCs that are integrated into the ASIC. Thus the readout architecture is embedded inside the detector volume resulting in very small number of connections to the DAQ system. Figure 3.4 presents a concept with only one DAQ link per active layer of the barrel module.

3.1.4 Physics Prototype

In order to gain experience in construction and operation of a high granularity calorimeter based on scintillating tiles with the WLS fibers readout a 1 m^3 physics prototype (PPT) was built in DESY within the CALICE calibration. A pre-prototype, referred to as MiniCal, was constructed and used to test the par-

ticle flow concept and to study hadronic showers. The readout for the MiniCal is realized either with the APDs or with the SiPMs.

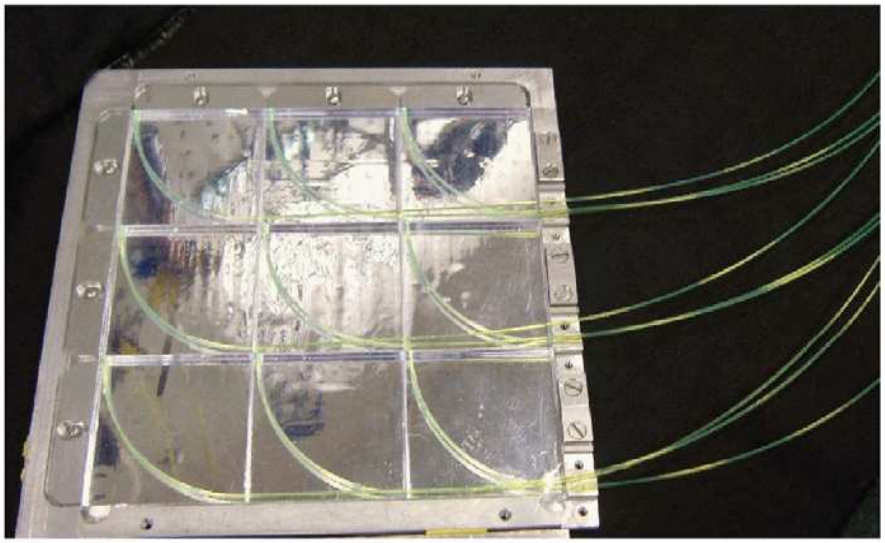

Figure 3.5: View of open cassette for the Minical with APD readout. Long WLS fibers for the light transport to the photodetectors are visible [23].

The MiniCal sampling structure consists in 28 layers of 2 cm thick stain-less steel absorbers interleaved with 0.9 cm thick gaps. The gaps are instrumented with thin aluminium cassettes carrying the scintillating tiles. Each cassette houses a 3×3 matrix of 5×5 cm^2 wide and 0.5 cm thick scintillators. Cassettes for the APD readout and those instrumented with SiPMs are depicted in Figure 3.5 and 3.6 respectively.

The MiniCal was successfully tested in an e^+ beam with range from 1 to 6 GeV both for the APD [23] and SiPM [24] readout. The studies of the hadronic shower development showed good agreement with Monte Carlo simulations. The energy resolution of $21\%/\sqrt{E\text{GeV}}$ was achieved. The success of the MiniCal opened the way towards the $1 \times 1 \times 1$ m^3 physics prototype.

The PPT contains altogether $\approx$ 8000 scintillator tiles with the SiPM readout. The device consists of 38 planes each housing 0.5 cm thick scintillating tiles of various area. The innermost region, covered with tiles of 3×3 cm^2, is surrounded with a lane of 6×6 cm^2 tiles and the edges are instrumented with 12×12 cm^2 tiles. The whole active area is covered with a plastic board that supports for optical fibers of the monitoring system and for the micro-coax readout cables. The connections between the readout cables and the SiPMs are realized by small PCBs. The response of individual tiles is monitored via LED light flashes. The fully equipped plane is depicted in Figure 3.7. Main parameters of the physics

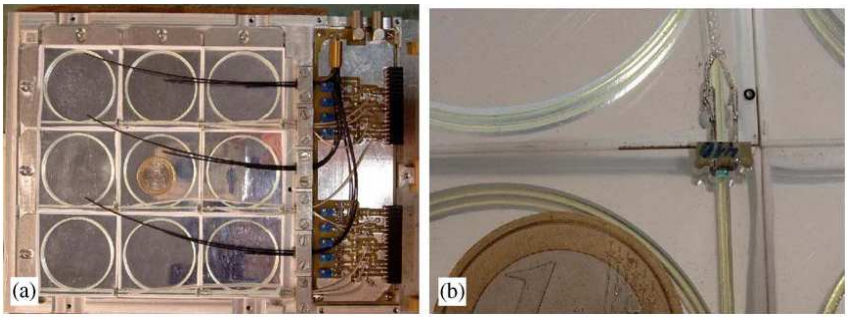

Figure 3.6: (a) A Minical cassette with the SiPM readout. (b) Zoom on the silicon photomultiplier attached to the tile. From [31].

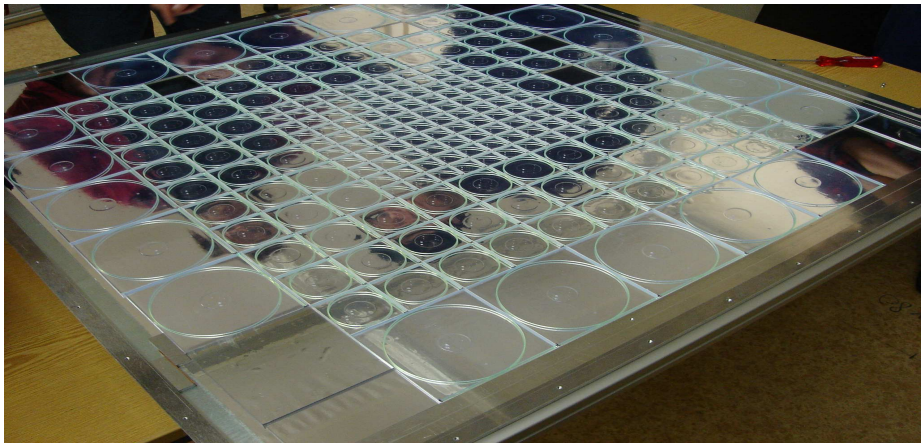

Figure 3.7: View of complete plane for the HCAL physics prototype [34].

prototype are presented in Table 3.4.

3.2 Calorimeter Calibration

The total number of channels to be calibrated corresponds to the total number of calorimeter cells, e.g. 204 000. The barrel contains 128 500, both endcaps 73 500 and both outer rings 2000 calorimetric cells. The response from the cells is required to be uniform for the cells of the same size and also across the cell area. The stability in cells response must be permanently monitored.

The reconstruction of the energy deposited in an individual calorimetric cell requires determination of several calibration coefficients. To convert the signal recorded in terms of ADC channels to energy in physics scale (GeV) the following calibration procedure for a cell i is proposed [25]:

	Layers 1-30 (per Layer)	**Layers 31-38** (per Layer)	**Total**
3×3 cm^2	100	–	3000
6×6 cm^2	96	121	3848
12×12 cm^2	20	20	760
Total	216	141	7608
Fibers in Bundle	$19(18+1)$	$19(18+1)$	$722(684+38)$
# Bundles	12	8	424
LED+PIN Diode	12	8	424
Total # Fibers	228	152	8184

Table 3.4: The fully equipped HCAL physics prototype module: summary of tiles, LED light distribution system and summary for the whole prototype.

$$E_i = (N_{ADC,i} - ped_i) \times \epsilon_i \times C^{ampl} \times C^{mass} \times C^{particle} \tag{3.1}$$

with E_i being the energy in GeV, $N_{ADC,i}$ the recorded signal and ped_i the pedestal. The calibration factors have the following meaning: ϵ_i deals with variations in gain of photodetectors, light yield, attenuation, photo cathode efficiency and corrects the ADC calibration differences. C^{ampl} is expressed in GeV/N_{ADC} and converts the measured signal, yet corrected with ϵ_i, to energy in the physics scale. C^{mass} corrects for fluctuations in cluster energy imposed by the inhomogeneity of the magnetic field and geometrical effects such as gaps or dead zones. $C^{particle}$ compensates for possible wrong determination of e/π response. A calibration procedure for the PPT (see Section 3.4.3) follows the general scheme (3.1) but the coefficients C^{mass} and $C^{particle}$ are not considered since they are related to the global detector environment.

3.2.1 Test Beam Calibration

The test beam calibration with muons, pions, electrons and protons is foreseen to be performed for several representative HCAL modules before the whole machine is mounted. The modules will be tested together with an ECAL prototype to achieve more realistic results. The calibration coefficients for the both devices are measured simultaneously since the calorimeter response is different for hadrons and electrons. The electromagnetic calibration is performed without the ECAL prototype in front.

3.2.2 Calibration with Real Events

A useful mean for the calibration is introduced by real detector events. Such a calibration is performed within the original magnetic fields and the whole calorimetric system in real position. A charged particle measured in the tracking system passing through the ECAL without any interaction is a sufficient

candidate for the direct calibration of the HCAL. The particle should have momenta higher than 2 GeV and the track separation in the ECAL should be at a level of 12 cm, i.e. there are no other overlaying clusters within the 12 cm radius around the track. Such particles have insufficiently small rates in a single cell thus to collect enough events for the calibration at least a one year period is necessary.

Another useful type of events are narrow jets originating from light quark-antiquark states. Measurements of energy and angle of jets can be calibrated in this way with beam energies up to 250 GeV. Jets from a single Z boson decay may be used for the energy calibration or to study the p_t balance. These jests are characteristic for their forward direction since the decaying Z boson is boosted by a high energy photon emitted along the beam axis. The Z boson production channel with the photon emission is dominant at collision energies of 500 GeV.

3.2.3 Calibration with Muons

Cosmic muons allow for the permanent online calibration. Number of muons hitting a single calorimeter cell per day is estimated to be higher than 6900 (4300) for muons with momenta above 4.5 (5.5) GeV. A calibration precision of $\approx 0.3\%$ can be achieved with such rates. Muons are identified independently from tracking information as MIP tracks in the whole calorimeter volume. The calibration with cosmic muons is only applicable for the barrel modules. A muon with momenta above 5.5 GeV is expected to cross the barrel cylinder shells of both the upper and lower modules but doesn't penetrate into the endcap modules. The tiles in the endcap modules are calibrated by means of beam halo muons. Due to the proper detector shielding the impact rate of beam halo muons is insufficiently small requiring a long time period for the precise calibration. Thus deticated endcap calibration runs with a defocused beam have to be taken to reach a calibration precision of 1% within one day.

3.3 Photodetectors

The photodetectors must allow first for operation in a very high magnetic field and second for covering wide dynamic range. A single calorimeter cell produces from about 65 photons when it is hit by a MIP particle to about 3.6×10^4 photons corresponding to an energy of about 50 GeV deposited in the cell.

Two types of photodetectors were considered for the HCAL: the avalanche photo diode (APD) and the silicon photomultiplier (SiPM). Both devices make use of an asymmetric p-n junction. As can be seen in Figure 3.8 a) the diode is connected in the inverse direction thus the electric field induced by the bias voltage is zero at the edges and reaches the maximum in the junction region. A photon hitting the diode creates electron-hole pairs which are stopped from the recombination due the electric field and start drifting toward the electrodes. Since the number of electron-hole pairs is proportional to the energy of the inci-

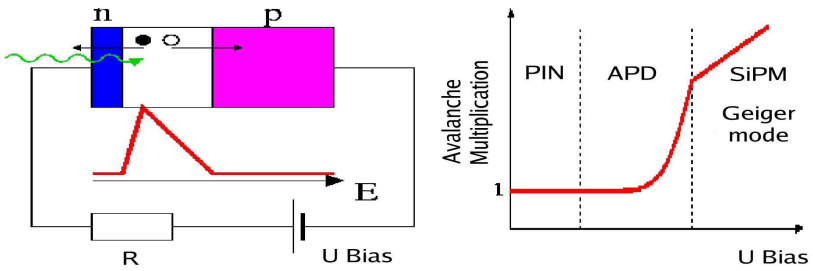

Figure 3.8: a) A basic circuit with a photodiode b) The gain dependence from the bias voltage. Two limits are depicted in the graph: the first stands for beginning of the avalanche mode and the second for the breakdown voltage where the Geiger mode starts [31].

dent photon the integral of the current pulse (e.g. the collected charge) induced by the drifting charges measures the deposited energy. Applying higher electric field leads to production of secondary electron-hole pairs which number (the avalanche multiplicity) is an important characteristics of the photodetector, the gain. Figure 3.8 b) shows the gain as a function of the applied bias voltage. While PIN diodes (see Section 3.4.1) are operated with no intrinsic gain APDs and SiPMs work in avalanche mode and Geiger mode respectively. Another important characteristics of photodetector are the quantum efficiency and the dark rate. The quantum efficiency expresses the probability that an incoming photon initiate the pair production. The dark rate concerns unwelcome signals originating in spontaneous pair production caused by temperature electron emission or non-signal photons. Number of oncoming photons necessary to create the avalanche is related to the photodetector sensitivity.

3.3.1 Avalanche Photodiode

APDs are widely used silicon based photodetectors with a thin sensitive area of $1 \times 1 - 5 \times 5$ mm^2 operated at bias voltage within a range from 100 V to 400 V achieving a gain from 1 to $\sim 10^4$. The quantum efficiency is sensitive to the wavelength of the incoming light and it is typically about 80% for the green light. A sketch of an APD is shown in Figue 3.9 a).

The APDs manufactured in Hamamatsu (S 8664-55) were studied for use in the HCAL [23]. These APDs have an active area of 3×3 mm^2 and are supplied with reversed biased voltage up to 425 V with gains of few hundreds. Their capacitance varies from 30 pF in the fully depleted state to 500 pF in

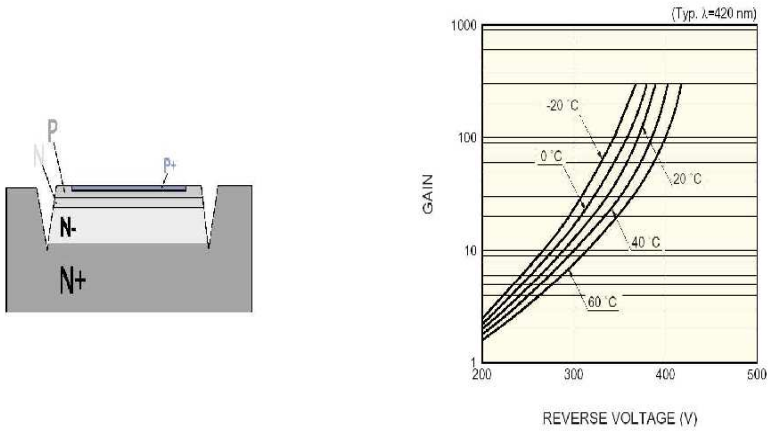

Figure 3.9: a) Schematic view of an APD b) APD gain bias voltage dependence measured at various temperatures [31].

the undepleted state. The low internal capacitance of few tens pF is favored for the fast readout since the signal length increases proportionally with the capacitance. Relatively low gain, compared to those of SiPM or vacuum phototubes, requires additional signal amplification. Inserting a preamplifier in front of the pulse shaper decreases the signal-to-noise (S/N) ratio therefore preamplifiers must be optimized for introducing minimum noise. The gain versus bias voltage dependence for various temperatures is presented in Figure 3.9 b).

3.3.2 Silicon Photomultiplier

The SiPM is an avalanche photodiode with the active surface of 1×1 mm^2 divided into more than 10^3 pixels. The device is operated in the limited Geiger mode with a reversed bias voltage that is 10-15% above the breakdown voltage. Individual pixels work as independent detectors each achieving a gain of $\sim 10^6$. To limit the current flow, e.g. to stop the avalanche, the bias voltage must be reduced below the breakdown voltage therefore each pixel is instrumented with a polysilicon resistor $R_{pix} = 400$ kΩ. The charge Q_{pix} accumulated in one pixel of capatitance C_{pix} determines strength of the signal: $Q_{pix} = \Delta V C_{pix}$.

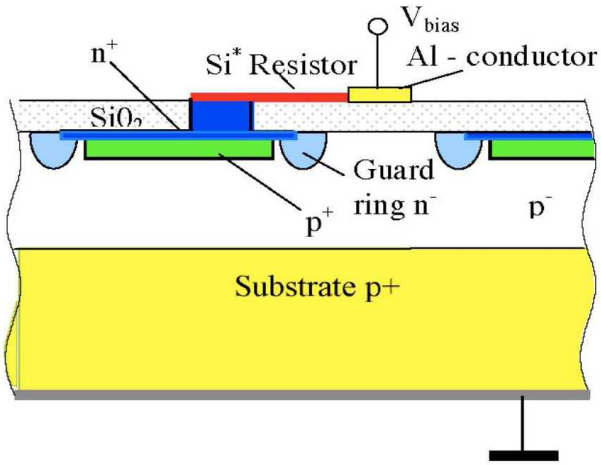

Figure 3.10: View of the silicon photomultiplier. Two single pixels (green stripes) surrounded by guard rings are sketched as being implemented into the common silicon substrate. From [31].

The capacitance is typically $C_{pix} = 50$ fF and the voltage difference $\Delta V = V_{bias} - V_{breakdown}$ is typically few volts which yields $Q_{pix} = 150$ fC, i.e. $\sim 10^6$ electrons. To reduce the crosstalk between adjacent pixels down to 20-30% each pixel is shielded with a guard ring. The lateral cross section of the device is shown in Figure 3.10.

Due to the Geiger mode the signal from a single pixel is independent from the number of incoming photons. The analogue information is obtained by summing all fired pixels. Thus the finite number of pixels limits the dynamic range of the detector which is observed as a non-linearity of a measured SiPM response function f_{resp}. The response function allows for conversion of the number of fired pixels into the number of photo-electrons:

$$N_{phe} = f_{resp}(N_{pix}) \tag{3.2}$$

Figure 3.11 shows the measured non-linear response for a SiPM with 1024 pixels/mm^2. The correction for the saturation effect can be performed either based on the parametrization of the measured response function or by introducing a model function similar to those successfully used for vacuum phototubes. The saturation function in the first order of expansion reads [26]:

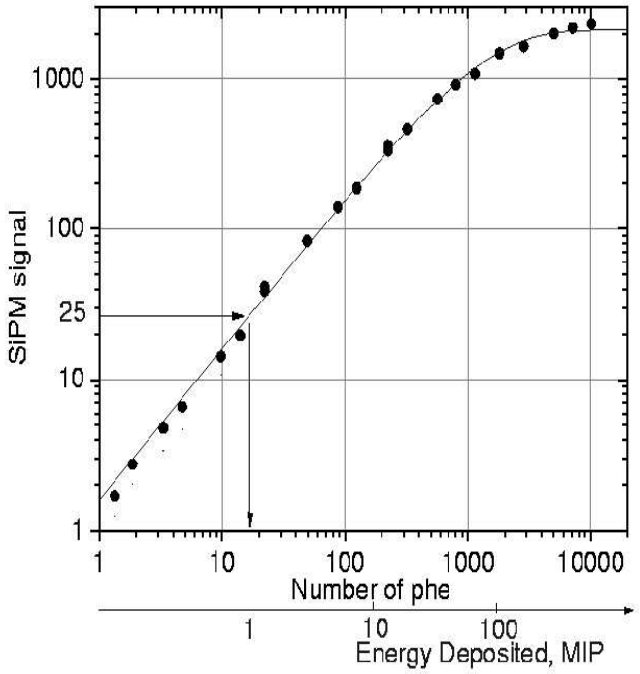

Figure 3.11: The measured response function for a 1156 pixels per mm^2 SiPM. The experimental points are overlaid with the saturation curve (3.3). The arrow shows that 1 MIP corresponds to 25 pixels fired [26].

$$N_{phe} = -N_0\left(1 - \ln\left(1 - \frac{N_{pix}}{N_0}\right)\right) \sim \frac{N_{pix}}{1 - \frac{N_{pix}}{N_0}} \tag{3.3}$$

with N_0 being the effective number of fired pixels.

Another important issue is the SiPM dependence with respect to temperature and bias voltage fluctuations. The gain temperature and bias voltage dependence is given by the manufacturer to be $\frac{dG}{dT} = -1.7\%/K$ and $\frac{dG}{dV} = 2.5\%/0.1V$. In fact the SiMP signal amplitude is a product of bias voltage and temperature dependent factors: SiPM gain, quantum efficiency and Geiger efficiency. Therefore the gain variations may rise up to $\frac{dG}{dT} = -4.5\%/K$ and $\frac{dG}{dV} = 7\%/0.1V$ as it was measured at room temperature [24].

Since the SiPMs are proposed to operate in a high magnetic field various measurements were taken to test for the SiPM behavior in magnetic fields up to 4 T [27]. The noise frequency, dark current, pixel cross talk and gain are found to be independent from the magnetic field. The signal amplitude recorded as a function of the magnetic field is constant with accuracy of 1% compared to that

taken at zero field.

3.4 LED Monitoring System

The online calibration with real events in the detector is not sufficient enough to ensure the permanent stability of the complete readout chain. A system based on LED or laser pulse light injection into the readout path is favored in many modern high energy detectors. Such a system allows for fast online control of individual electronic channels since the light is injected repetitively in the time gaps between bunch crossings. The LED based concept which was successfully operated in the H1 SPACAL calorimeter [28] is considered for the HCAL.

The silicon based photodetectors in question (SiPMs and APDs) show gain variations especially due to temperature and high voltage fluctuations. Note that the stability of the power supply is better than 10^{-4} thus the photodetectors gain is dominantly influenced by temperature changes. Both the WLS fibers and scintillating material are liable to aging effects resulting in reduced number of photons delivered to photodetectors. Aging decreases also the quantum efficiency of photodetectors. The acquired data are corrected to these effects based on information from the monitoring system. The light injection system must provide intensities in range from few photoelectrons up to 100 MIPs to control the SiPM response function.

3.4.1 Light Emitting Diode

LEDs are compound semiconductor (gallium-arsenide) diodes. A low voltage applied on the rear contacts of the p-n junction makes electron-hole pairs recombine which is followed by energy release in form of photons. The LED is demanded to provide short light pulses (10-20 ns) in order to simulate a signal induced by a real particle. A special LED driver was developed for this purpose. The LED is reversed biased with short periodical switches of polarity. This is realized by means of a capacitor parallel-connected to the LED. After the capacitor is loaded the trigger signal opens the field effect transistor (FET) gate and the capacitor is discharged through the LED within $\approx$ 15 ns. The repetition rate for this process is typically of 1 kHz. The basic circuit of the LED driver is depicted in Figure 3.12(a). The light pulse has typically a rise time of 3 ns and a fall time of 12 ns. The pulse shape recorded by a fast photomultiplier (PMT) is presented in Figure 3.12(b).

The emitted light intensity has maximum at wavelength of about 400 nm. A sample of five LEDs was measured [29] to check for uniformity in the light emission. All the tested LEDs show similar wavelength distribution with the peak at 440 nm (Figure 3.13(a)). The spectra keep their form also under changing the light intensity(Figure 3.13(b)). The intensity of the emitted light is being changed by applying different current in range from 20 μA to 100 mA. Various LED properties such as linear behavior of the light intensity with respect to

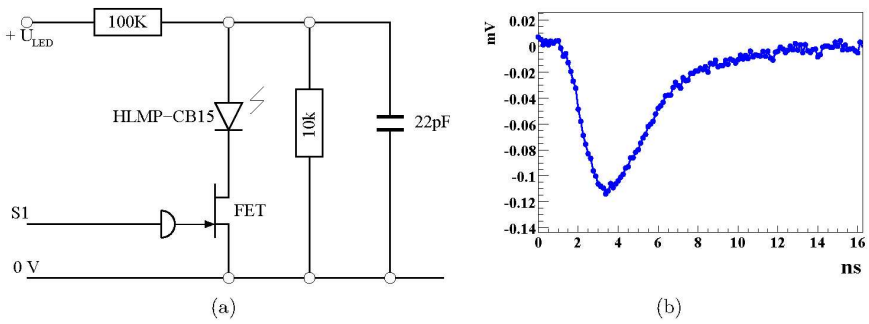

Figure 3.12: (a) Diagram of the basic LED driver circuit.(b) The LED pulse detected with a fast PMT [31].

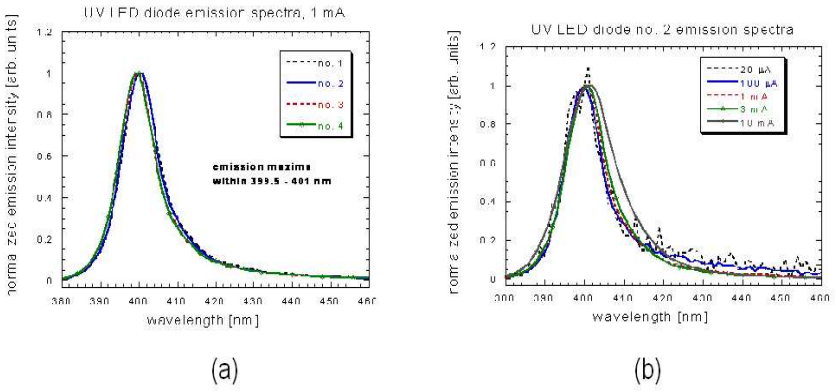

Figure 3.13: (a) Emission spectra of 5 different LEDs. Uniformity in wavelength of the emitted light is perceptible with the peak at 440 nm for all LEDs. (b) Emission spectra of a single LED with measured for various intensities, amplitudes are displayed in the relative scale [29].

the input voltage, light emission inhomogeneity or temperature stability was measured in dedicated experiment described in detail in Chapter 4.

3.4.2 Setup

The scheme of the full readout chain for a single tile with integrated LED monitoring is depicted in Figure 3.14. A single LED is supposed to inject light into several photodetectors (APDs or SiPMs) at once. Since the LEDs might show amplitude variations due to temperature fluctuations, aging effects or instabilities of the pulse shape an additional control of the LED performance is provided by a PIN diode.

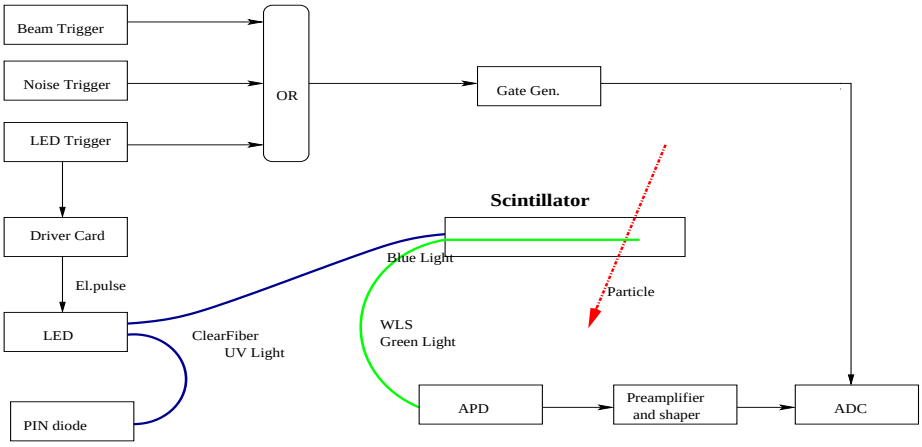

Figure 3.14: The signal readout scheme instrumented with the LED monitoring system. An incoming particle hits the scintillation tile producing blue light that is collected by a WLS fiber and delivered to an APD (or a SiPM). The tile is also connected to the LED emitting blue light to simulate particle induced scintillation. A PIN diode monitors for LED stability. The gate for the ADC is generated either by the beam trigger (a real event) or the LED trigger (LED light flash).

The PIN (p-i-n) photo diode has an intrinsic layer between the p and n region. It is a stable photodetector operated at low bias voltages with no internal amplification, e.g. with a gain equal to 1. The output signal is almost temperature independent (0.18%/K) within the wavelength range from 300 nm to 500 nm.

The physics prototype for the HCAL involves the SiPM readout technology. The light injection system for each plane of the prototype is operated with one calibration and monitoring board (CMB) developed in Prague [30]. The CMB integrates the LED driver electronics and carries the PIN diodes. Additional sensitive preamplifiers are necessary to overlap the gain difference between the PIN diode and the SiPM since they use a common readout electronics. The CMB is instrumented to allow for communication with the DAQ system and the slow control. Each board houses 12 LEDs and the same number of PIN diodes.

3.4.3 Calibration with LED Light

Calibration procedures established for the MiniCal with the SiPM readout has been applied to the HCAL physics prototype. The calibration is based on separation of the MIP peak from the pedestal peak which allows to translate the measured number of ADC channels into a deposited energy in MIPs. This scheme is often referred to as a light yield (LY) calibration. The LY is the MIP amplitude expressed in number of fired pixels with measured value of ≈ 15 pixels/MIP.

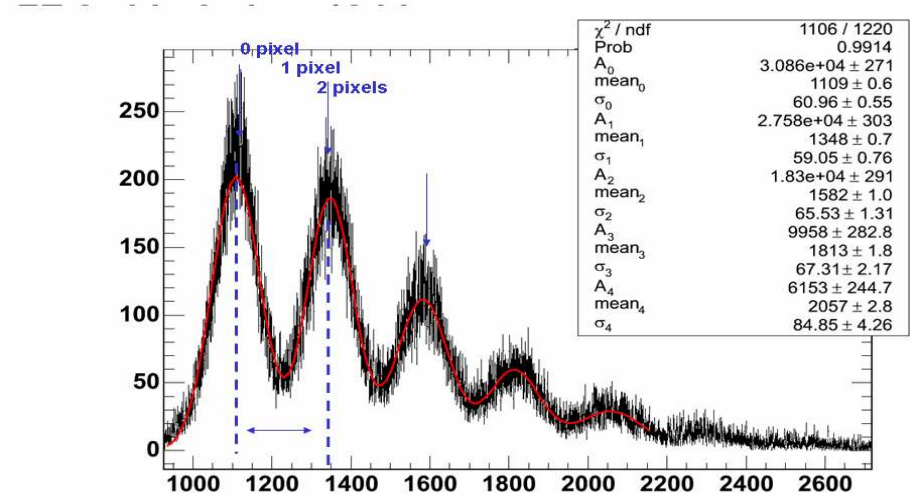

Figure 3.15: SiPM response to the low intensity LED light with the first peak being the pedestal and the other peaks corresponding to 1,2, etc. pixels fired. The vertical axis displays number of collected events and the horizontal axis is scaled in ADC channels (12-bit ADC were used for data acquisition) [34].

The MIP signals can be collected either with cosmic muons or with a large spread muon or hadron beam but the calibration of the all cells takes several hours in the both cases. Alternatively the LY can be determined from the SiPM pixel gain. The gain is extracted by separation of two neighboring peaks in spectrum that is obtained when the SiPM is illuminated with low intensity LED light. The SiPM response with single pixel signals is shown in Figure 3.15. To achieve a precision of 1-2% for the gain determination $\sim 10^5$ events have to be acquired which requires about 20 min assuming a 100 Hz DAQ rate limit.

The calibration procedure for the PPT follows the general scheme proposed in Section 3.2 omitting the global calibration coefficients. Giving the light yield and the measurable SiPM response function f_{resp} the calibration for the tile i proceeds according to the equation [26]

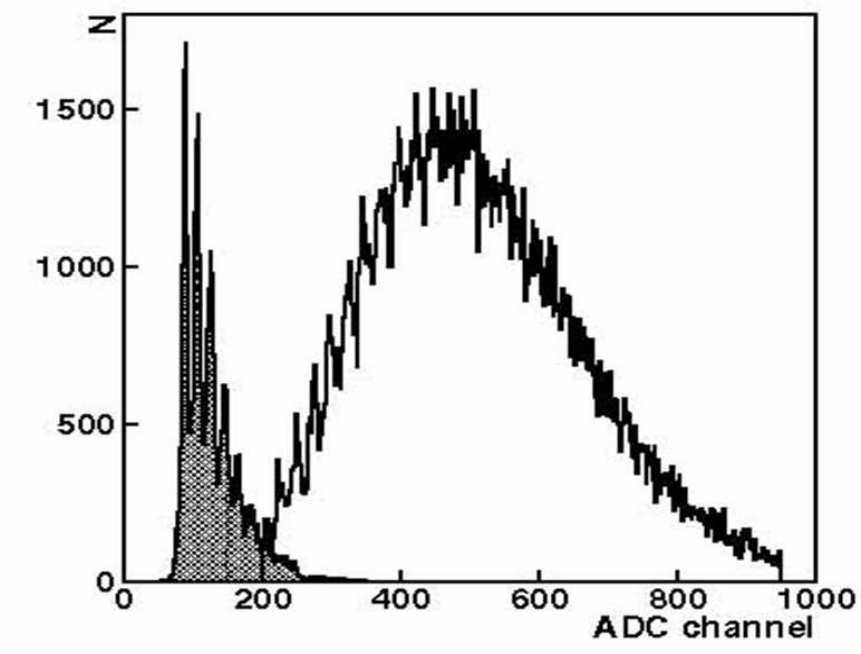

Figure 3.16: Comparison of the SiPM low intensity light response (shaded histogram with distinguishable single photo-electron peaks) to a typical MIP signal (open histogram) [35].

$$E_i[\text{MIP}] = f_{resp}\Big(A_i[\text{MIP}] \times LY_i\Big[\frac{\text{pixel}}{\text{MIP}}\Big]\Big) \times \frac{1}{LY_i'} \tag{3.4}$$

with $LY_i'[\text{ph.e./MIP}]$ [1] $= f_{resp}(LY_i[\text{pixel/MIP}])$ and $A_i[\text{MIP}] = \frac{A_i[\text{ADC}]}{A_i^{MIP}}$ being the amplitude expressed in units of MIP. A typical MIP signal from a single tile together with low intensity LED light response is depicted in Figure 3.16. In order to optimize the single pixel peaks separation the VFE electronics runs in so called calibration mode with a high preamplifier gain of $\sim$ 90 mV/pC and a short ASIC chip shaping time of $\sim$ 40 ns. Although the 40 ns shaping time minimizes the SiPM dark rate it is not sufficient to acquire the physics data. To meet the test beam trigger latency which is typically of $\sim$ 150 ns the VFE electronics is operated with a shaping time of $\sim$ 200 ns and a preamplifier gain of $\sim$ 9 mV/pC in the physics operation mode. When extracting the LY an inter-calibration factor I_{phys}^{calib} must be accounted for:

$$LY_i = \frac{A_i^{MIP}}{G_i} \times (I_{phys}^{calib})_i \tag{3.5}$$

[1] ph.e. stands for number of photoelectrons

with G_i being the SiPM single pixel gain.

3.4.4 Stability Monitoring

A threefold monitoring system is designed to be used in the HCAL and it is studied with the PPT. The slow control system monitors the temperature in each PPT plane by means of five sensors and controls the SiPM bias voltage. Another stage of the monitoring concerns measurements of the SiPM gain which are performed with the low intensity LED light at the beginning of each run. Finally the tiles are being continuously illuminated with medium intensity LED light and the peak position of the response signal is permanently monitored. Figure 3.17 shows a sketch of the fully equipped plane.

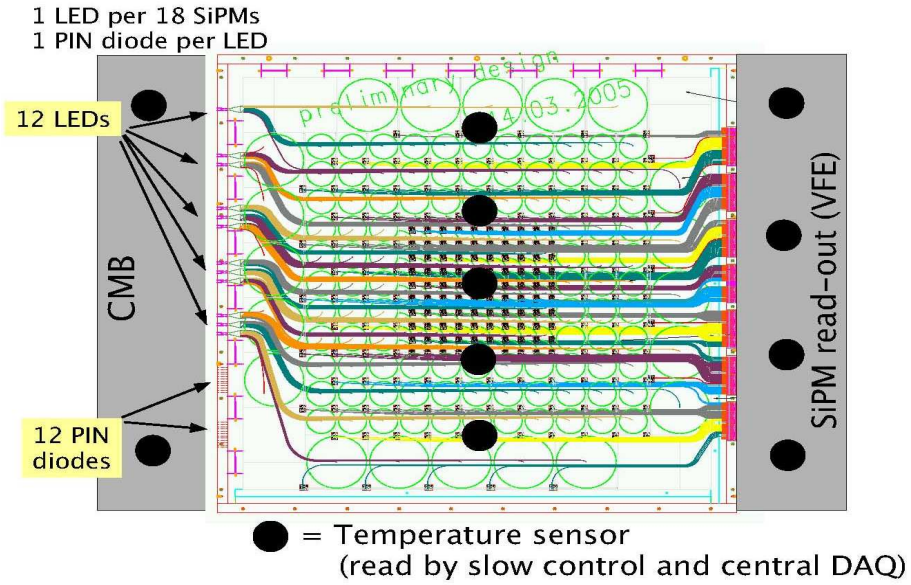

Figure 3.17: The PPT plane assembled with the light distribution system and the temperature sensors. The CMB board, mounted on the left side, is equipped with 12 LEDs from which the light is distributed to all tiles in the plane and to 12 PIN diodes. The optical fibers and the readout cables are displayed as thin color lines, the green circles represent WLS fiber loops in individual tiles. The readout board, attached from the right side, houses the VFE for the SiPM readout [36].

An example of temperature correction for the measured signal is given in the following. Assuming small temperature changes the gain variation can be described with a linear function. For the measured signal A the variation is

expressed as

$$\frac{1}{A}\frac{dA}{dT} \approx \frac{\alpha}{T} \tag{3.6}$$

where α is extracted from measured photodetector temperature dependencies, e.g. for APD $\alpha = 4.5\%$. The correction for the temperature dependence can be written in general as:

$$A(T) = A(T_0) + (T - T_0)\frac{dA}{dT} = A(T_0)(1 + \Delta T\frac{1}{A(T_0)}\frac{dA}{dT}) \equiv A(T_0)C(T) \tag{3.7}$$

According to (3.6) the correction coefficients can be written as

$$C(T) = 1 - \alpha\frac{\Delta T}{T} \tag{3.8}$$

The LED reference signal A_{LED} is PIN diode corrected with $f(\frac{PIN(T_0)}{PIN(T)})$ thus the correction coefficients $C(T)$ are determined as

$$C(T) = \frac{A_{LED}(T)}{A_{LED}(T_0)} \times f\Big(\frac{PIN(T_0)}{PIN(T)}\Big) \tag{3.9}$$

Long term measurements performed with the Minical [31] showed that correction of temperature correlated dependencies can be performed according to (3.9) with remaining effects below 0.5%.

Chapter 4

LED Selection Test

This chapter reports measurements I performed in a laboratory at Institute of Physics of the ASCR, Prague. The experiment is dedicated to the LED monitoring system (see Section 3.4) that is foreseen to be used within the large detector concept for the future linear collider for stability monitoring and calibration of the hadronic calorimeter. Results of the measurements were presented at CALICE collaboration Meeting in Montreal [37].

4.1 Introduction

Tests with fully assembled $1 \times 1 \times 1$ m^3 hadronic calorimeter prototype involve calibration and monitoring with the LED light injection system. Readout of the optical signal is realized with SiPM which imposes a requirement for a wide range of light intensities to be delivered by LEDs. While the low intensity light corresponding to few photo electrons serves for the light yield extraction high intensities are demanded to correct for the SiPM non-linear response at 80-100 MIPs. Therefore it is necessary to ensure uniformity of light intensities from different LEDs. It is sufficient enough to demand a maximum 100% spread of the light intesity across all channels, e.g. the intensity is constrained with $I_{max} \leq 2I_{min}$. The constrain for LEDs themselves is much narrower in fact since about 70% of the intensity variation is ascribed to mechanical effects of the light guide system (fiber bendings, coupling gaps, etc.). LEDs that aspire to assembly the detector must be uniform in the light emission within a 30% spread, e.g. with a constrain $I_{max} \leq 1.3I_{min}$.

The calorimeter prototype is foreseen to be instrumented with 38 active layers each operated with 12 LEDs. The task of this thesis is the measurement of the spread of the light intensity for a sample of 872 LEDs in order to select a set of LEDs sufficient for the prototype. The light intensity variations of individual LEDs originate mainly in a spread of parameters during the production. A dedicated setup with an APD readout was built for the purpose of this selection test.

4.2 Experiment Setup Layout

The light intensity of a tested LED is measured with APDs and the signal is displayed in an oscilloscope. A bundle of optical fibers is used to deliver light from the LED to the photodetector. Schematic drawing of the setup can be seen in Figure 4.1.

The tested LED is powered with a driver that served as prototype for the CMB board used in the PPT (see Section 3.4.2). The driver has two inputs: first a trigger signal synchronizing the light emission and data acquisition, referred to as T-Calib, and second low voltage controlled by a potentiometer within range from 0 to 5 V, referred to as V-Calib. The intensity of emitted light is proportional to the height of the pulse that is generated in the driver. The pulse height is controlled by means of the potentiometer. The LED is inserted into

a cylindrical light adapter made of dark dural and can be roted along its axis. The LED is an inhomogeneous source of light therefore the response signal is sensitive to the angle of rotation.

The emitted light is led via clear plastic fibers from Kuraray with 1 mm diameter. The bundle contains 12 fibers of $\sim$ 1 m length. Since the device is designed to simulate conditions in the real detector the fibers are not optically isolated. The downstream ends of several fibers are attached to a mask containing four APDs (S 8664-55 spec) from Hamamatsu. The from the APD is preamplified and shaped before being sent to the data acquisition unit. Because of the expected temperature dependence of the APD gain temperature monitoring is performed with a micro-amperemeter connected directly to the APD mask. The APDs are powered with a high voltage (HV) of 270 V which corresponds to the gain at a level of $\simeq 10$. Since the stability of the HV supply is better than 0.1% the gain variation related to HV fluctuations is neglected.

The signal from the APD is displayed on a digital phosphor oscilloscope (Tektronix TDS 5104). The oscilloscope has a bandwidth of 1 GHz and allows to read simultaneously four channels, this limits the number of fibers from the bundle to be read out. Figure 4.2 shows a cross section of the bundle with four selected fibers marked with different colors. Fibers from both the middle and the edges of the bundle were selected. This choice follows the requirement to cover the whole area of the LED emission with its light inhomogeneity.

The waveforms of signals from the four fibers as displayed with the oscilloscope can be seen in Figure 4.3. The relevant information is either the amplitude (pulse hight) or the integrated area of the pulse. The area has a meaning of the total collected charge divided by the APD resistance and it is typically from 10 to 30 nVs. Since the light intensity is proportional to the collected charge the measured area is used in further analysis. These parameters are extracted from waveforms averaged over 10^4 signals and stored in a PC. Additional information like pulse fall and rise time is stored as well. The repetition frequency of the CAMAC is typically 1 kHz thus about 10 s are necessary to acquire 10^4 LED pulses. Such a short time of a single measurement avoids time instabilities.

In order to ensure that the number of only four fibers can bring relevant results 9 fibers were measured with a 10-channel CAMAC equipped with 10-bit ADCs. Angular characteristics (similar as in Section 4.3.4) were scanned for these fibers and were found to correspond to the measurement with the oscilloscope [38].

4.3 Measurements of Setup Properties

Before the selection test is performed various basic properties of the setup were measured. Five etalon LEDs were randomly chosen from the whole sample for this purpose.

First the reproducibility of measurements was checked. A tested LED is inserted into the light adapter by hand from which systematical uncertainty arises that has to be included in a total error estimation.

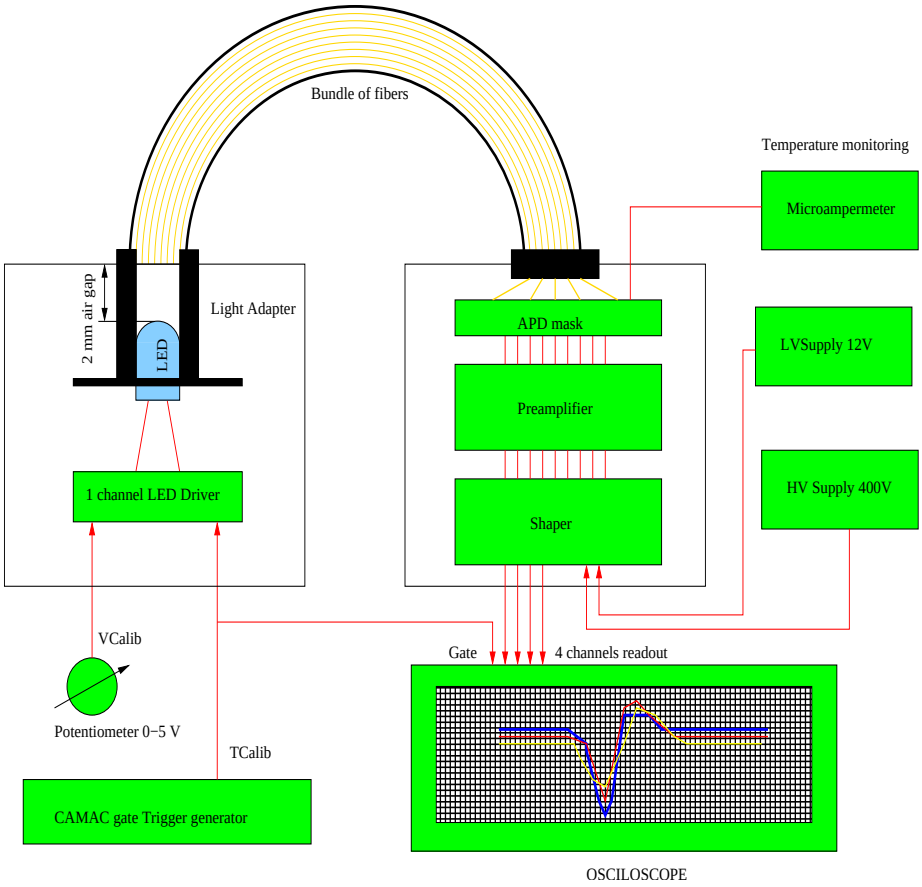

Figure 4.1: Sketch of the setup for the LED selection test. The LED is coupled to the bundle of fibers and it is powered with the LED driver that receives T-Calib (trigger) and V-Calib (emitted light intensity control) signals. The T-Calib is generated in the CAMAC and ensures coincidence between the LED pulse and data acquisition. The downstream end of the bundle of fibers is coupled to a box containing the APD mask and signal processing electronics (preamplifier, shaper). The high voltage supply powers APDs, the microamperemeter serves for temperature monitoring and the low voltage powers the electronics itself. The signal is displayed with the four-channel oscilloscope.

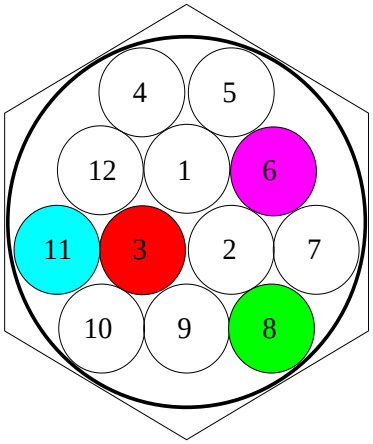

Figure 4.2: Cross section of the bundle of fibers. The colored fibers are read by an oscilloscope. The topology of the selection follows the requirement to cover the whole cross section of the bundle.

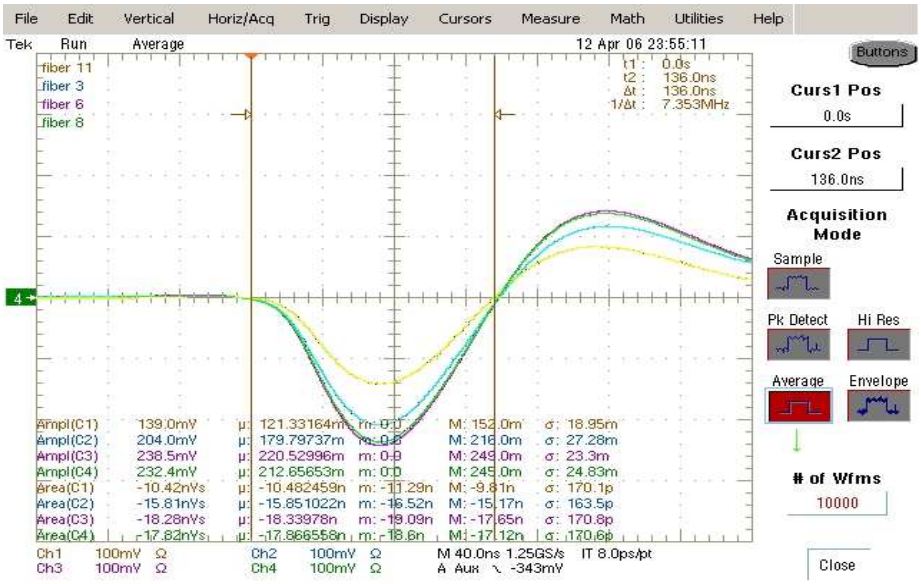

Figure 4.3: Typical signals on the oscilloscope with four different readout channels. Pulses from fibers corresponding to the choice according to Figure 4.2 can be seen. Cursors (the vertical lines in the display) show an interval (the gate) where the charge that is proportional to the light intensity is integrated. The gate width is set to 136 ns to cover the full pulse width.

Since the APD gain is temperature dependent a dedicated measurement was taken to extract coefficients for temperature correction.

The emitted light is not homogeneous due to internal geometry of the LED. A millimeter size chip that is responsible for the light emission is not centered with respect to the LED cap. Therefore different response signals for fibers are observed when an LED is rotated around its axis.

Not only the light inhomogeneity causes that each fiber carries a different fraction of the total intensity. If the bundle is illuminated with homogeneous light variations in signals from individual fibers are observed as well. These variations originate in different quality of individual fibers, optical contacts to APDs and possible crosstalk between fibers. The task of calibration measurement is to unify the response from individual fibers.

The intensity of light of an LED should be proportional to the driver pulse height which is controlled by means of the V-Calib signal adjustable with the potentiometer. The linear response to the V-Calib in range from 0 to 5 V was checked in dedicated measurement.

4.3.1 Reproducibility and Error Estimation

In order to estimate the precision of the measurements one LED had been inserted into the light adapter repeatedly. the spread of this measurement serves as estimation of systematical error from reproducibility. This error should reflect uncertainty of inserting an LED into the light adapter.

Figure 4.4 shows the measured area for the all fibers. The estimated errors for each fiber are summarized in Table 4.1. Systematical errors are at level of 6% for each fiber which is sufficient enough for the selection purposes.

	μ [nVs]	σ_{sys} [nVs]	δ_{sys} [%]
Fiber 3	10.33	0.52	4.99
Fiber 6	16.53	1.01	6.14
Fiber 8	21.02	1.23	5.85
Fiber 11	21.83	1.02	4.65

Table 4.1: Results of reproducibility measurements: the mean value μ with the absolute systematic variation σ_{sys} and the corresponding relative error δ_{sys} are presented for each fiber.

When the selection test is performed total number of 872 areas $\{A_i\}$ is acquired each burdened with both statistic and systematic uncertainties:

$$\sigma_i^2 = (\delta_{stat} A_i)^2 + (\delta_{sys} A_i)^2 \tag{4.1}$$

The relative statistic error is given by two contributions: first the precision level of the oscilloscope (value given by the manufacturer is $\sim 1\%$) and second the electronic noise at level of $\sim 1\%$. The statistic error is than estimated as $\delta_{stat} = 2\%$ which is typically lower than the systematic error.

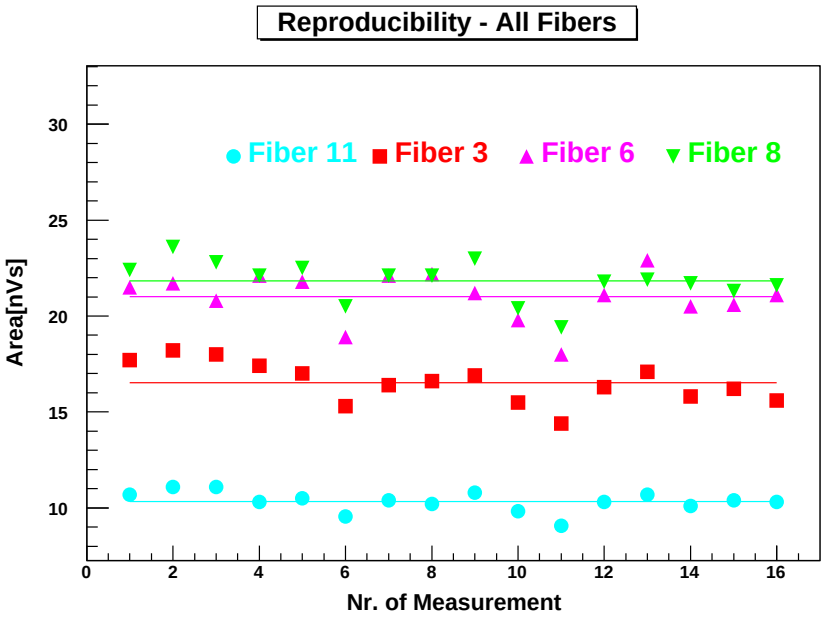

Figure 4.4: Measurement of reproducibility with one LED. The response from the four selected fibers is depicted. Altogether 16 measurements were performed, points at the x-axis are not equidistant in time. The measured areas are fitted with constant lines for each fiber.

4.3.2 Temperature Dependence

The long term observation of temperature fluctuation in the laboratory room (in order of several K) gives an idea of temperature stability of the device. Temperature dependence of the measured amplitude is expected since the gain of APDs is sensitive to temperature changes. The gain fluctuations of $\sim 2\%/K$ are expected at room temperature for the gain of ~ 10 [39]. Due to relatively small temperature fluctuation a linear model for the measured temperature dependent area $A(T)$ is supposed:

$$A(T) = A_0(t_0 T + t_1) \tag{4.2}$$

where A_0 is a temperature independent amplitude; t_0, t_1 are parameters of the linear fit and T is the temperature in K. Introducing coefficients $C(T) = t_0 T + t_1$ the formula for the correction can be written as

$$A_{TCorr} = \frac{A}{C(T)} \tag{4.3}$$

with $C = t_0 T + t_1$ and A_{TCorr} being the temperature corrected area. The fit results are shown in Figure 4.5. The obtained t_0, t_1 parameters values are summarized in Table 4.2.

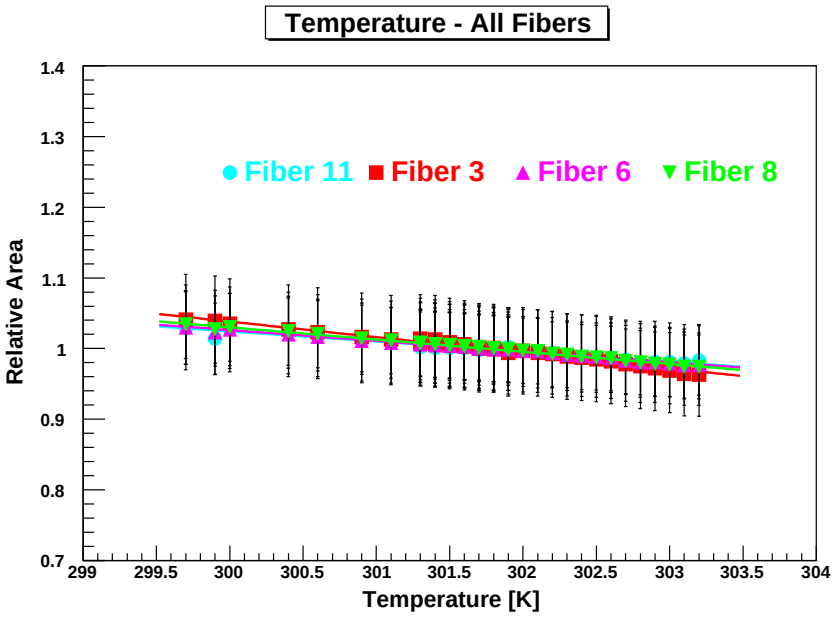

Figure 4.5: Measured temperature dependence of the area for all fibers. The area is displayed in relative scale, the errors includes both systematic and statistic uncertainties according to (4.1). The experimental points are fitted with formula (4.2). The response varies approximately from +5 to -5% in a range of $\Delta T = 4$ K.

	$t_1(10^{-2})$ [1/K]	$\sigma_{t_1}(10^{-2})$ [1/K]	t_0	σ_{t_0}
Fiber 3	-1.43	0.06	5.31	0.17
Fiber 6	-2.21	0.05	7.66	0.16
Fiber 8	-1.52	0.04	5.58	0.12
Fiber 11	-1.73	0.03	6.22	0.11

Table 4.2: Fit results for the measured temperature dependence with supposed linear behavior. The parameters t_0, t_1 with corresponding errors are listed for each fiber.

The temperature dependence of the LED itself is not considered for this correction. Measurements of individual tested LEDs were short-time ($\sim$ 1 min) and before each measurement the system was stabilized. The stable conditions were achieved in a closed box after 70 hours from the start of the electronics system. Long term temperature instability of the LED was measured later with a PIN diode to be $\pm 0.5\%$ [38].

4.3.3 Calibration

Fractions of light intensity in individual fibers are different for homogeneous light which is an effect of the whole optical and electronics system. Although the APDs are supplied with the same voltage they work with different gains (see Figure 4.7) which results in different signals in individual channels of the preamplifier. The variations in response are also caused by different properties of individual fibers, optical linking between fibers (note that the fibers are not isolated inside the bundle) and optical contacts to the APD (gaps between downstream ends of fibers and the APDs are not the same).

Ideally the total intensity I_0 is distributed evenly such that each fiber carries the same intensity I which can be expressed as

$$I_0 = IN_{fib} \tag{4.4}$$

with N_{fib} being the number of selected fibers. Light intensity I_i carried by a fiber i is corrected with the calibration coefficients c_i:

$$I = c_i I_i \tag{4.5}$$

Taking into account that $I_0 = IN_{fib} = \sum_{j=1}^{N_{fib}} I_j$ the relation for the calibration coefficients c_i reads:

$$c_i = \frac{\sum_{j=0}^{N_{fib}} I_j}{N_{fib} I_i} \tag{4.6}$$

The light homogeneity is simulated by increasing a distance between the LED and the bundle. The air gap dividing the LED and the fiber bundle termination is now enlarged from original 2 mm to 70 mm so that the cross section of the light cone is small enough to assume the light to be homogeneous. The decrease of the intensity within the 70 mm gap is acceptable since the signal is still visible on the oscilloscope and measurable with a sufficient accuracy. The calibration coefficients are evaluated according to 4.6. Note that although the relation 4.6 is written for intensities the measured areas are inserted instead without any impact on the final result due to proportionality between the area and intensity. The calibration coefficients are presented in Table 4.3. As can be seen in Figure 4.10 the influence of the calibration to the final selection is very small (red and yellow points, representing calibrated and uncalibrated data resp., are almost overlapping).

	c_i
Fiber 3	0.876
Fiber 6	1.076
Fiber 8	1.221
Fiber 11	0.910

Table 4.3: Calibration coefficients for individual fibers. The coefficients were computed based on measured areas according to equation (4.6).

4.3.4 LED Angle Anisotropy

The asymmetry of the light source with respect to the LED central point is a consequence of the LED construction. The center of the light emission should be located in an ideal case in the LED axis but in fact it is displaced. The measurement of the Φ dependence of the light emission was done in order to know the anisotropy in the light emission of the LED.

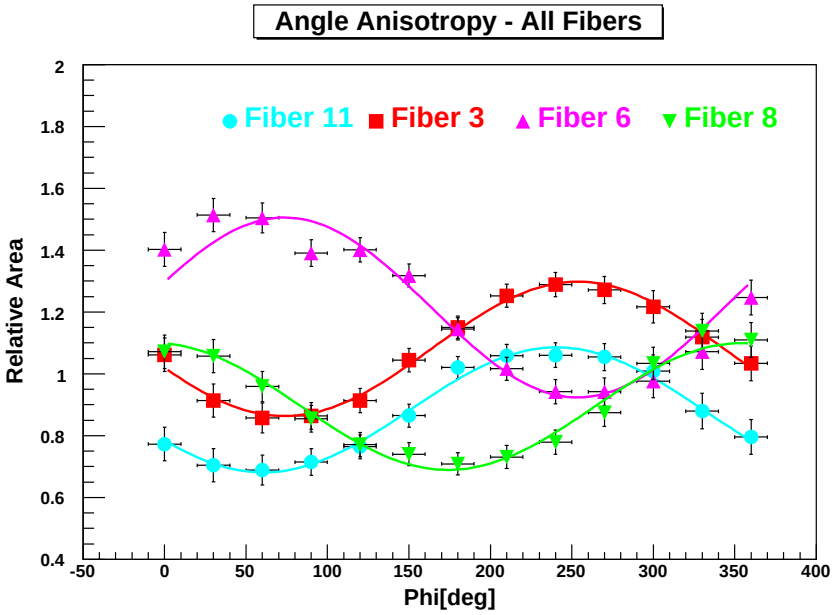

Figure 4.6: Dependence of the measured area on the LED axis orientation with respect to the entry point of the bundle of fibers. The area is displayed in the relative scale. The experimental points are fitted with a sine function with different Φ-offset for each fiber.

The LED was rotated in order to illuminate the bundle at various positions in whole 360° interval. The rotation angle step was 30°. Excluding the systematic errors like electronic noise or imprecision in inserting the LED into the light adapter the measured light emission asymmetry should copy the internal structure of the LED. Therefore the values within the whole 360° region are expected to be fitted with a sine curve. Inaccuracy in inserting the LED into the bundle under the certain angle is estimated to be $\pm 10°$. Results are presented in Figure 4.6 where can be seen that the sine curve fits the data within reasonable accuracy.

The phase shift in response signal obtained in this measurement confirms the assumption that the source of the light emission is not placed in the LED axis. Due to this fact the reproducibility of measurements with this setup is very sensitive to the insertion of a sample LED with the exact angle of 0° into the

fiber bundle fixture. This gives rise to the systematical error of the measured area at the level of 6%.

4.3.5 Linearity of LED Response

The requirement for any LED is that the intensity of emitted light should be proportional to the input driving current. The V-Calib signal that is being changed with the potentiometer (see Figure 4.1) in the range from 0 to 5 V is transformed through resistances in the integrated circuit of the driver. The LED driving current is proportional to the generated pulse height which roughly corresponds to the voltage delivered by the V-Calib. The response signal which is proportional to the total collected charge from the APDs should be a linear function of the V-Calib supposing the LED linear behavior. As can be seen in Figure 4.7 the measured response increases linearly with the V-Calib signal for the all channels in a range from 3.5 to 5 V[1].

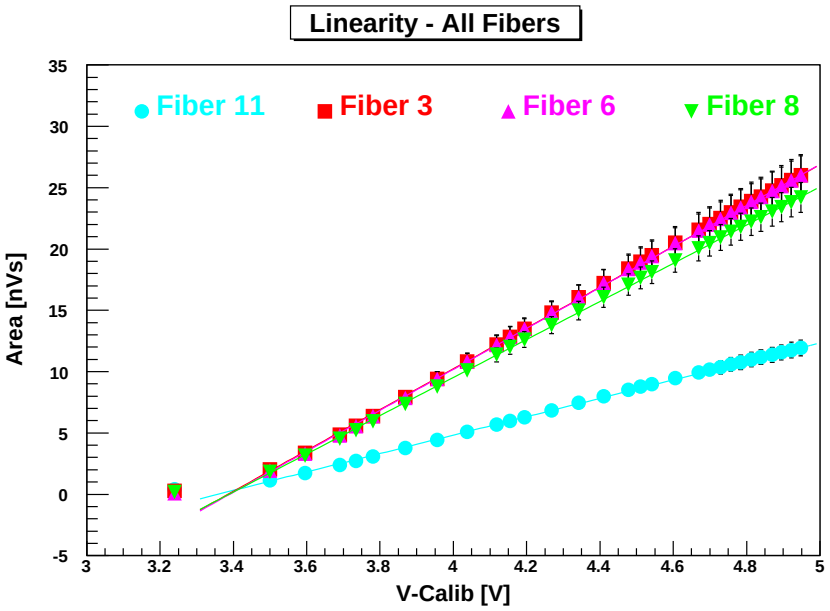

Figure 4.7: Measured area vs. V-Calib signal dependence. A good linearity behavior of an etalon LED can be seen from the linear fit in the range from 3.3 to 5 V. Different slopes of the lines for individual channels are caused by different gains of APDs.

[1]LEDs have a threshold of the emittance at about 3.5 V.

4.4 LED Selection

Having checked for basic properties of the experimental setup and extracted coefficients necessary for corrections the selection test itself can be performed. Each LED of the sample is inserted into apparatus once and the response area is recorded. The low voltage value is fixed to 4 V and the temperature is permanently monitored.

The selection is based on the requirement that a sufficient LED emits light of intensity constrained with $I_{max} \leq 1.3 I_{min}$ which means that a spread around the mean intensity of the sample must be less than $\pm 15\%$. The measured areas that are proportional to the light intensity are translated into the relative scale and are distributed into a histogram with a mean value of 1. The $\pm 15\%$ criterion is applied to cut off insufficient LEDs.

4.4.1 Decrease of Response Signal

After working out the response from all measured LEDs a decrease of the measured areas occurred at the beginning of measurements which is quite evident from Figure 4.8. It turns out that the obtained areas cannot be sufficiently fitted with a constant line which should represent the mean value of the area distribution. The data rather suggest a long term mild decrease. The temperature dependence is already included in the applied corrections so the decrease might be caused either a loss of the gain in the APDs or by electronics system instability. The four different APDs were operating simultaneously and all together showed rather the same effect. As the properties of the APDs are well known they give no reason to expect such behavior. The driver chip card controlling the LED operation appears to be a possible candidate to explain the decreasing effect. The driver was connected immediately after it had been constructed so the aging of parts such as resistors, condensers, diodes, etc. might cause the long term decrease of signal. After a certain time period the aging effect almost disappeared and the signal kept rather constant. This assumption offers to fit the data with a 'broken line'

$$f(x) = \Theta(x_0 - x)(ax + b) + \Theta(x - x_0)(ax_0 + b) \tag{4.7}$$

with a, b, x_0 taken as fitting parameters and x representing the ordering number of an LED (corresponding to a time scale). Results of the fit are summarized in Table 4.4.

Figure 4.8 shows the measured amplitudes for a single fiber fitted with function (4.7). As can be seen in the picture the parameter x_0 divides the sample into two parts: the first one with the linear decrease of amplitude and the second one with the time independent amplitude. As can be seen in Table 4.4 the fitted values of the parameter x_0 have a very small fiber to fiber variation. As a relevant sample dividing parameter the average of x_0 over the all fibers was used - the dividing point is the LED number 638. In our model all the LEDs with number higher than 638 can be considered without the aging effect. The second part could have been taken as the relevant data set but the cut off would has

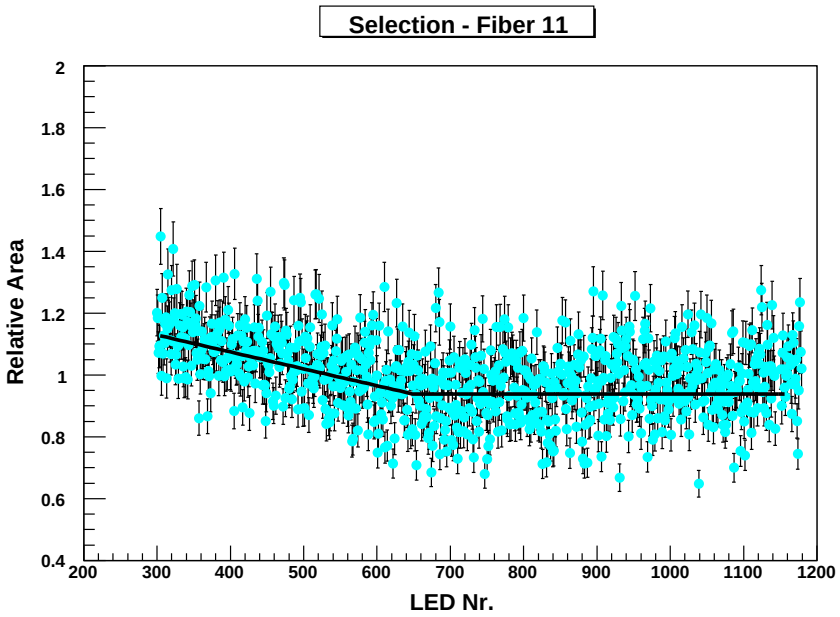

Figure 4.8: The whole sample (872 pieces) of LEDs after the temperature correction, calibration and normalization. The measured relative areas are fitted with function (4.7). The response from the fiber 11 is displayed here, results for the remaining fibers are summarized Table 4.4.

discarded about one half of the whole sample. The data were corrected using the 'broken line' model (4.7) instead. Proceeding in the similar way as for the temperature dependence one obtains a correction formula:

$$A_{corr} = A\frac{ax_0 + b}{ax + b} \tag{4.8}$$

The corrected data for the all four fibers and for the whole sample of 872 LEDs are displayed in Figure 4.9.

4.4.2 Selection

The main criterion for the selection itself is the total amount of light that a tested LED is able to deliver. Taking the average area over four fibers the most complete information is obtained for this purpose. Figure 4.10 shows the measured area averaged over four fibers in various stages of correction: the normalized data, the data after the temperature correction and the data after the calibration. The almost overlapping points indicate the small influence of the performed corrections to the final results of the selection. The data are displayed without the correction for the aging effect.

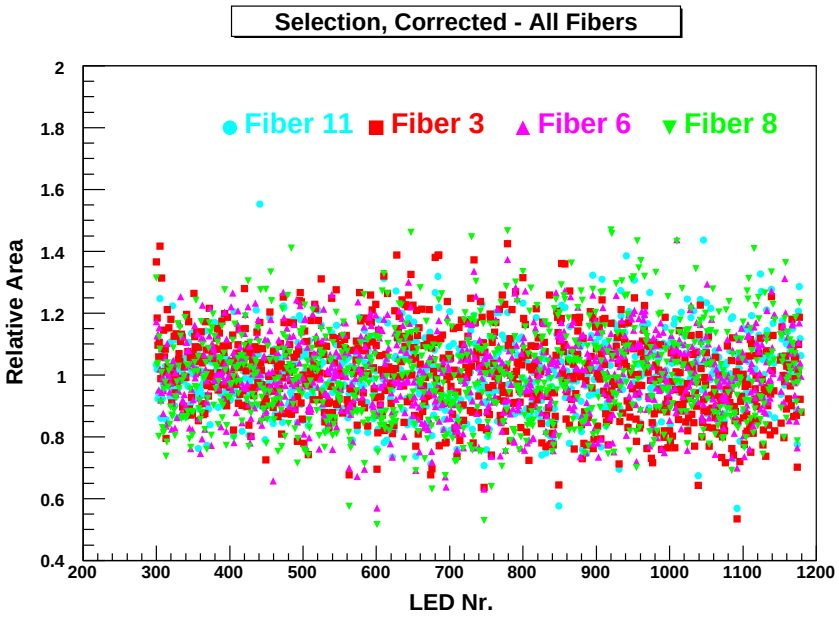

Figure 4.9: The whole sample of LEDs corrected with respect to the amplitude decrease caused by the aging effect.

The histogram based on which the selection is performed is presented in Figure 4.11. The acquired areas from the whole sample are first corrected for temperature fluctuations and for different response from individual fibers (calibration) and subsequently the correction for the aging effect is applied. The areas are then normalized and averaged over the all fibers. These values are distributed into the histogram.

Results of the selection with various criteria are summarized in Table 4.5. The number of LEDs whose response satisfy the 15% criterion is 749.

	$a(10^{-4})$	$\sigma_a(10^{-4})$	b	σ_b	x_0	σ_{x_0}
Fiber 3	-5.93	0.61	1.33	0.03	632	2
Fiber 6	-9.98	0.39	1.59	0.02	642	2
Fiber 8	-4.45	0.50	1.26	0.03	640	2
Fiber 11	-6.27	0.67	1.34	0.03	640	2
Average					638	

Table 4.4: The fit results for the aging correction. Fitted values of the parameters a, b, x_0 from formula 4.7 are listed with corresponding absolute errors for each fiber. Averaged value of x_0 over the four fibers is added.

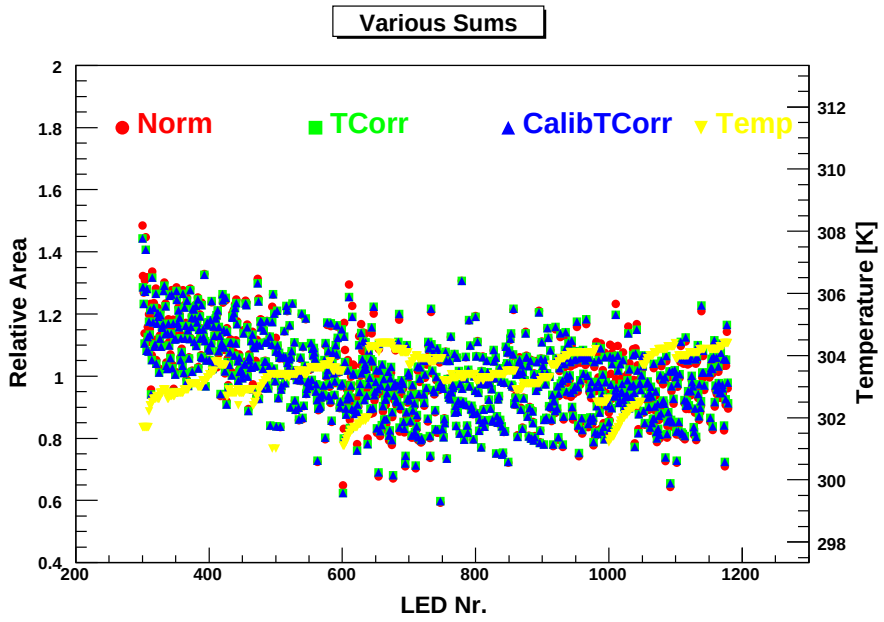

Figure 4.10: The signal (represented as relative areas) from four fibers characterized by the mean value of the four readout channels. The signal without the temperature correction and calibration, just normalized, is denoted as Norm (red points), the temperature corrected points as TCorr (green squares) and the temperature corrected and calibrated points as Calib TCorr (blue triangles). In addition the temperature, denoted as Temp (yellow triangles), for each measurement is depicted. Note that this picture is not corrected with respect to the aging effect discussed in Section 4.4.1.

4.5 Summary

The whole sample of 872 LEDs was measured and analyzed. The LEDs show acceptably reasonable properties: light emission characteristics are almost the same across the whole sample and the emitted light intensity is proportional to

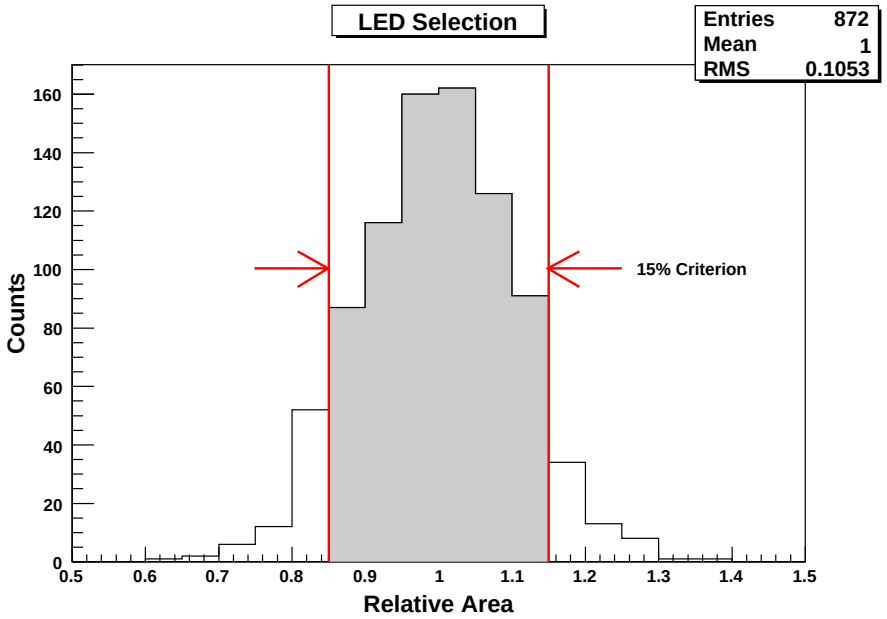

Figure 4.11: A histogram of relative areas which are computed as mean values of the areas in the four readout channels. The chosen part of LEDs satisfying the selection criterion ($\pm 15\%$) is displayed as a shadowed part of the histogram.

Criterion	**Selected**	I_{max}/I_{min}
$\pm 5\%$	317	1.11
$\pm 10\%$	562	1.22
$\pm 15\%$	**749**	**1.35**
$\pm 20\%$	829	1.5

Table 4.5: Selection results - number of selected LEDs for different criteria (with $\pm 15\%$ being the key criterion) and corresponding ratio of the maximum to minimum intensity.

the input current.

To check for the basic properties of the experiment setup five etalon LEDs had been chosen. By means of these etalon LEDs the basic characteristics like the reproducibility of measurements, influence of the light inhomogeneity effects or temperature dependence of the APDs gain were measured.

During the measurements the decrease of response signal occurred which was ascribed to instability of electronics caused by aging. The correction with the function of a form of a 'broken line' was applied for each of four readout channels.

The 15% criterion based on requirements for the whole optical system con-

strained the sample down to 749 LEDs (about 86% of the original sample) that were accepted for the further use in the physics prototype of the hadronic calorimeter.

Chapter 5

Conclusion

Experiments at the ILC are foreseen to resolve many questions imposed by the SM (problem of the Higgs boson, precise measurements of coupling constants, etc.) or those related to possible new physics (e.g. supersymmetry, grand unification). Any advance of particle physics is conditioned by development of new generation of particle detectors. Physics at energies foreseen at the ILC significantly exceeds possibilities of present detectors , e.g. the jet energy resolution is demanded to be two times better than at LEP. A worldwide effort is dedicated to accomplishment of detection techniques dealing with issues such as simulations of performance, integrating detector subsystems, development of fast readout technologies or coding new reconstruction algorithms.

Four different detector concepts are proposed to deal with the challenge that the ILC imposed to the particle detectors construction. Calorimetry within these concepts includes various options all characterized by unprecedented high granularity. The scintillation based hadronic calorimeter is favored among others due to novel photodetectors, SiPMs, that can be integrated directly inside the detector volume bringing thus significant simplification of the readout architecture. Scintillation particle detection technique also suggests calibration and monitoring of the detector with an external source of light. Such a calibration is fast and independent from beam or cosmics events.

The scintillator tile hadronic calorimeter is foreseen to be equipped with a versatile calibration and monitoring system involving UV LEDs. Thu full readout chain including scintillation tiles, wavelength shifting fibers and photodetectors is monitored by means of LED light injection into individual tiles which simulates particle induced scintillation. The physics prototype with integrated LED monitoring system was built in order to prove the technological principle and address issues for further development.

The complete LED calibration and monitoring system requires a large number of UV LEDs. The wide range of energies (up to 100 MIPs) that the LEDs are supposed to cover in the sense of the particle event simulation leads to the demand on the uniformity in the light emission among all involved LEDs. A set of $\sim$ 900 LEDs was purchased to assembly the physics prototype. It was a key task of this thesis to work out the whole sample of the LEDs which included measurements of same basic characteristics of the LEDs and exclusion of LEDs whose light intensities overflow the uniformity criterion.

It was measured that the emitted light intensity of LEDs is proportional to the input current which is crucial for an easy control of the monitoring system. About 85% LEDs from the whole sample were selected thus the uniformity in the light emission is acceptable. The measurements established a procedure for the LED selection based on APD readout and acknowledged that commercially accessible UV LEDs are a reasonable choice for calibration and stability monitoring in calorimetry.

Bibliography

[1] TESLA Technical Design Report (March 2001), http://tesla.desy.de/new_pages/TDR_CD/start.html

[2] T. Hambye, K. Riesselmann. Phys. Rev. D55:7255, 1997.

[3] B.W. Lee, C. Quigg, H.B. Thacker. Phys. Rev. 16:1519, 1977.

[4] D.R.T. Jones, S. Petcov. Phys. Lett. B84:440, 1979

[5] J. Ellis, M.K. Gaillard, D.V. Nanopoulos. Nucl. Phys. B106:292, 1976

[6] International Linear Collider Reference Design Report (February 2007), http://media.linearcollider.org/rdr_draft_v1.pdf

[7] R. Brinkmann, G. Materlik, J. Rosbach and A. Wagner (eds.), Conceptual Design of a 500 GeV e^+e^- Linear Collider with Integrated X-ray Laser Facility, DESY-97-048 and ECFA-97-182, 1997: http://www.desy.de/lccdr/tesla/tesla.html.

[8] P. Chen and K. Yokoya, Beam-Beam Phenomena in Linear Colliders, KEK-report 91-2, 1991.

[9] I. Hinchliffe et al. Phys. Rev., D55:5520, 1997; ATLAS: Detector and Physics Performance Technical Design Report, Volume 2. CERN/LHCC/99-15, ATLAS TDR 15.

[10] http://www.interactions.org/imagebank/

[11] Large Detector Concept Outline Document, 2006

[12] Tesla Technical Design Report, Part IV: A Detector for TESLA, 2001

[13] International Linear Collider Reference Design Report, 2007

[14] The SiD Concept Group: SiD Detector Outline Document, 2006

[15] GLD Concept Study Group: GLD Detector Outline Document, 2006

[16] The 4th Concept Study Group: Detector Outline Document, 2006

[17] J.C. Brient: On the calibration of the W-Si ECAL proposed for TESLA, LC-DET-2001-057, 2001

[18] J.C. Brient et al.: Si-W Calorimeter Performances. LC-DET-2001-058, 2001

[19] The digital HCAL project in CALICE, http://polywww.in2p3.fr/activites/physique/flc/HCAL_digital.html

[20] F. Kirchner, B. Gastinaeu, V. Kliokhine, Y. Pabot: The TESLA Detector Magnet, LC-DET-2001-056, 2001.

[21] D. Schulte: Study of Electromagnetic and Hadronic Background in the Interaction region of the TESLA Collider, TESLA 97-08, 1996.

[22] S.M. Xella Hansen, D.J. Jackson, R. Hawkings, C.J.S. Damerell: Flavour Tagging Studies for the TESLA Linear Collider, LC-PHSM-2001-024, 2001.

[23] V. Andreev et al.: A high-granularity plastic scintillator tile hadronic calorimeter with APD readout for a linear collider detector, 2006.

[24] V. Andreev et al.: A high granularity scintillator calorimeter readout with silicon photomultipliers, 2004.

[25] V. Korbel, V. Mongunov: Calibration and Monitoring of the TESLA Tile Hadronic Calorimeter, LC-DET-051-2001, 2001.

[26] Nicola D'Ascenzo et al.: CALICE scintillator HCAL commissioning experience and test beam program, LC-DET-2006-009, 2006.

[27] E. Garutti et al.: LC note, LC-DET-2004-025, 2004.

[28] J. Janoth: Das Calibrationssystem CAM fur das neue Kalorimeter SpaCal des Detektors H1 bei HERA und Analyse erster Daten, HD-IHEP-96-17

[29] Measurements of LED properties performed by S. Nemecek, Institute of Physics AS CR, Prague, May 2004.

[30] Ivo Polák, Prague, CALICE Colaboration, meeting at the Nothern Ilinois University, 2005.

[31] Hendrik Meyer: Studies of avalanche photo diodes for a calorimeter readout at a linear collider detector, 2004.

[32] V. Korbel: The Optical and Electronic Readout of the HCAL Tile Calorimeter, LC-DET-2001-52, 2001.

[33] V. Korbel: Optimization studies for a scintillator-tile to wavelength-shifter fiber light readout for the TESLA-Calice Tile-HCAL, LC-DET-2004-28, 2004.

[34] J. Cvach: Scintillator HCAL prototype commissioning and calibration, Institute of Physics AS CR, 2006.

[35] E. Garutti: Calibration and Monitoring of the Analog HCAL prototype, International Linear Collider Workshop, Standford USA, 2005.

[36] S. Schätzel: SiPM HCAL Stability, DESY, 2006.

[37] Jaroslav Zálešák: UV LED quality test, CALICE Collaboration Meeting, MsGill Uni, Montreal, Canada, presented on May 11, 2006, http://www.hep.physics.mcgill.ca/XHEP/ILC/calice/meeting/

[38] Jaroslav Zálešák: private communications.

[39] Henri Dautet et al.: Photon counting techniques with silicon avalanche photodiodes, APPLIED OPTICS/Vol.32, No. 21, 1993